**DE GRUYTER** Open Geosciences 2024; 16: 20220618

**Research Article**

Erteng Wang, Xinwei Zhai*, Yaoshen Huang, Chengze Li, Ruihuan Su, Lei Wu, Gaorui Song, Zhiang Guo, Wanfeng Chen, and Jinrong Wang

# Permian tectonic switch of the southern Central Asian Orogenic Belt: Constraints from magmatism in the southern Alxa region, NW China

https://doi.org/10.1515/geo-2022-0618
received September 19, 2023; accepted January 28, 2024

**Abstract:** Late Paleozoic plutons are widely distributed in the Alxa region, southernmost Central Asian Orogenic Belt, and provided an important clue in constraint for the closing time of the Paleo-Asian Ocean (PAO). In this article, we present new zircon U-Pb ages and whole-rock geochemical data from the Permian Huoersen and Zongnaishan plutons in the southern Alxa region. The Huoersen gabbro (ca. 285 Ma) is enriched in large-ion lithophile elements and depleted in high-field strength elements, similar to the features of continental marginal arc. They were most likely generated by partial melting of depleted mantle that was modified by subduction metasomatic fluids. The Zongnaishan granites (ca. 267 Ma) show characteristics of I-type granites and were generated in a syn-collision setting. The Huoersen granites (ca. 259 Ma) are peralkaline and have positive $\varepsilon_{\mathrm{Nd}}(t)$ (+1.2 to +1.5) values, exhibiting $A_2$-subtype granites affinities. They were formed by melting of lower crust in post-collision extension setting. Based on geodynamic mechanism, a three-stage evolution model is delineated: subduction, syn-collision to post-collisional extension for oceanic branch of the PAO during the Permian. In general, the rock assemblages indicate a tectonic switch from subduction to post-collision extension regimes and the final closure of the PAO.

**Keywords:** geochemical, Permian, tectonic switch, Alxa region, Central Asian Orogenic Belt

## 1 Introduction

Plate tectonic is the predominant process of global tectonic, and its main forms are oceanic subduction-closure and subsequently continental collision [1–3]. The Central Asian Orogenic Belt (CAOB), one of the largest mega-accretive orogenic belts in the world, is bounded by the Eastern European Craton to the east, the Tarim Craton and North China Craton to the south, and the Siberia Craton to the north (Figure 1a) [4–7]. The CAOB is a collage of geological bodies formed in subduction closure of the Paleo-Asian Ocean (PAO) during Neoproterozoic to Mesozoic, which is regarded as one of the significant geological events during the global plate tectonic [8–11]. Recent researches show the PAO was finally closed in the Tianshan-Solonker suture zone, southern CAOB [12]. However, compared with the eastern and western parts of the CAOB [13–20], less attentions are paid for the middle part and further study is vital and necessary.

The Alxa region is located in the southernmost margin of the middle CAOB (Figure 1a) and bounded by the Solonker suture zone to the east and Tianshan-Beishan suture zone to the west (Figure 1b) [12,21]. Magma and tectonic activities of the Alxa are strong, and it is characterized by an abundance of the acid and mafic-ultramafic magmatism (Figure 1c) [20,22,23]. For a long time, the closure time of the PAO in the Alxa region has been highly controversial, such as in the middle to late Devonian [24],

---

*** Corresponding author: Xinwei Zhai,** School of Earth Science, Key Laboratory of Mineral Resources in Western China (Gansu Province), Lanzhou University, Lanzhou, 730000, China, e-mail: zhaixw926@lzu.edu.cn
**Erteng Wang, Ruihuan Su, Lei Wu, Gaorui Song, Zhiang Guo, Jinrong Wang:** School of Earth Science, Key Laboratory of Mineral Resources in Western China (Gansu Province), Lanzhou University, Lanzhou, 730000, China
**Yaoshen Huang:** Chongqing Earthquake Agency, Chongqing, 404100 China
**Chengze Li:** PetroChina Research Institute of Petroleum Exploration and Development-Northwest, Lanzhou 730000, China
**Wanfeng Chen:** College of Geography and Tourism, Hunan University of Arts and Science, Changde, 415000 China

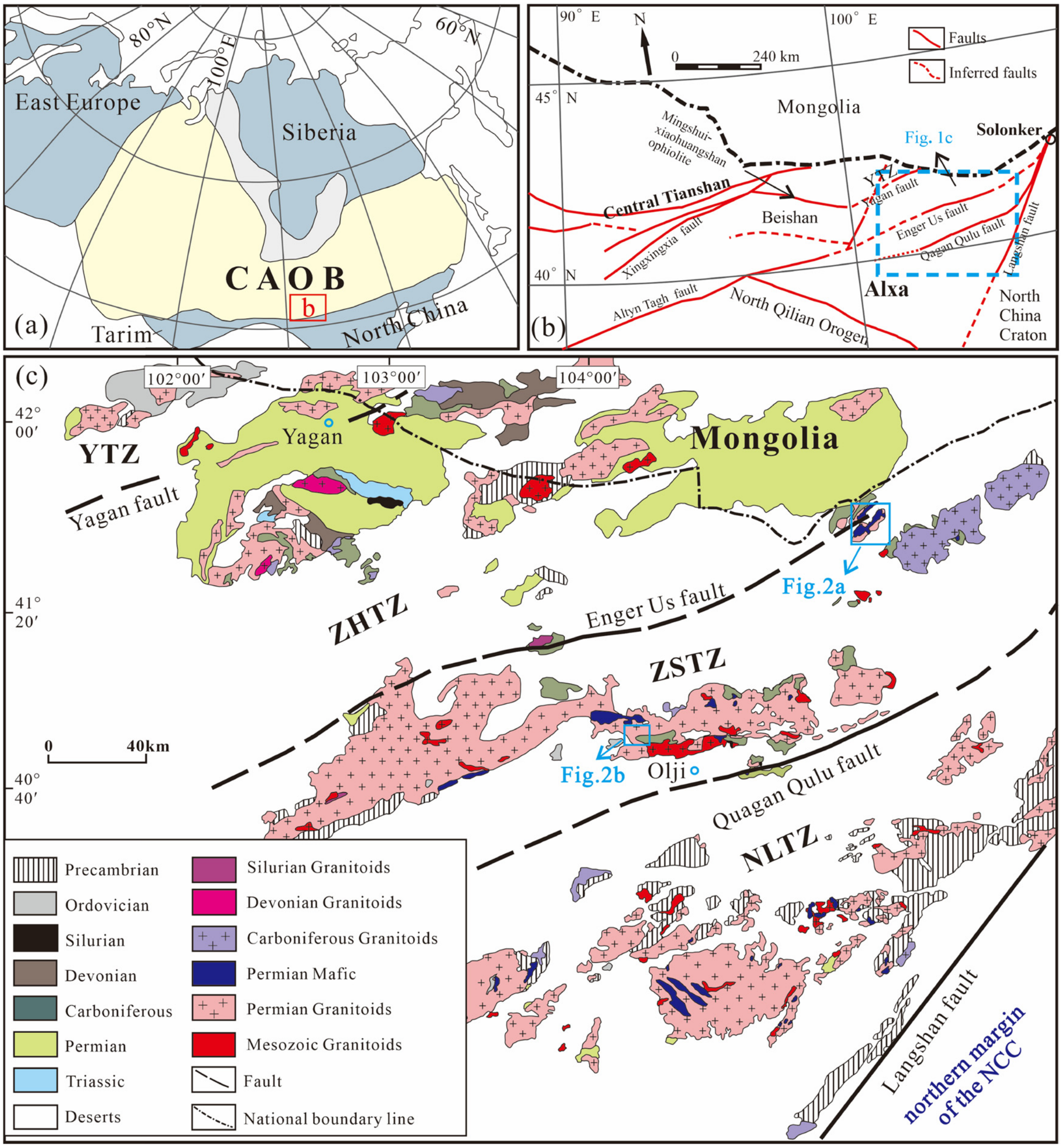

**Figure 1:** (a) The location of the Alxa region in the simplified tectonic sketch map of the Central Asian Orogenic Belt (modified after [5]). (b) Tectonic outline of the surrounding Alxa in North China (modified after [64]). (c) Geological map of the Alxa region (YTZ – Yagan tectonic zone, ZHTZ – Zhusileng-Hangwula tectonic zone, ZSTZ – Zongnaishan-Shalazhashan tectonic zone, NLTZ – Nuoergong–Langshan tectonic zone, modified after [71]).

or late Carboniferous to early Permian [20,25,26], and subduction of the PAO until the middle Permian to early Triassic [27] (and others references). Notably, the Paleozoic tectonic transformation from subduction to post-collision was widely manifested by magmatism related to subduction and closure of the PAO in the southern Alxa region [22,28,29]. So, to better constrain the timing of subduction and closure of the PAO, a detailed study of Alxa region rocks' assemblage is important.

Here, we report continental marginal arc gabbro, I- and A-type granites about subduction, syn-collision to post-collision setting in the Zongnaishan-Shalazhashan, southern Alxa region. We present geochronological, geochemical, and Sr–Nd–Hf isotopic data for the granite and gabbro. We further discuss their petrogenesis and the deep-level processes relating to the magmatic activity and thus provide constraints on the evolution of the Alxa region and the timing of the closure of the PAO branch.

## 2 Geological setting

The Alxa region, belonging to the southernmost part of the CAOB (Figure 1a), is located at the intersection of Tarim Craton, North China Craton, and Qilian Orogenic belt, which was initially regarded as an eastern extension of the North China Craton (Figure 1b) [30,31]. In particular, through the restoration of metamorphic, paleomagnetism, and mélange, the Alxa region showed an inconsistent tectonic history with the North China Craton [32].

The Alxa region has four major tectonic zones, e.g. Yagan tectonic zone, Zhusileng-Hangwula tectonic zone, Zongnaishan-Shalazhashan tectonic zone, and Nuoergong–Langshan tectonic zone from north to south, and divided by three major faults and ophiolite belts: the Yagan fault, the Enger Us fault (ophiolite belt), and the Qugan Qulu fault (ophiolite belt) (Figure 1c). The Enger Us Ophiolite Belt might represent the major oceanic branch of the PAO, with the age of 300 Ma [33,34], while the Qugan Qulu Ophiolite Belt (ca. 275 Ma) [34] is a back arc basin, which is formed by the southward subduction of branch PAO and had closed during the late Paleozoic [10,27,35].

In the southern Alxa region, the desert-covered area has a crystalline basement of Neoproterozoic Granite gneiss, which is mainly distributed in Nuoergong–Langshan tectonic zone [36]. The limestone and dolomite of Cambrian to Ordovician are sparsely distributed, while the Upper Paleozoic strata are very common (Figure 1c). The Devonian strata are clastic-carbonate sedimentary formation of neritic facies, and the Carboniferous to Permian strata major are conglomerate, sandstone, carbonate rock, volcanic rock, and pyroclastic rock [30,37].

Late Paleozoic Granites are widespread with less basic rocks in the Alxa region (Figure 1c). The corresponding tectonic environments are of great dispute, and previous studies gave different ideas: active continental margin environment [19,23,35,38], the intraplate setting [39], or post-collision extensional environment [20].

## 3 Sample descriptions

The Huoersen pluton and the Zongnaishan pluton are located at the Zongnaishan-Shalazhashan tectonic zone, south of the Enger Us Ophiolite Belt (Figure 1c). The Huoersen pluton consists of granite and gabbro, and the gabbro was intruded into by granite (Figure 2a). The Zongnaishan pluton consists of granites and intruded into the Carboniferous strata (Figure 2b). We sampled Huoersen granite, Huoersen gabbro, and Zongnaishan granite for analysis of geochronology and whole rocks geochemistry.

The grayish-black Huoersen gabbros (Figure 3a) with gabbro-structure are mainly composed of plagioclase (55%), pyroxene (20%), amphibole (20%), and iron (<5%). The plagioclase grain is euhedral to subhedral. The pyroxene is allotriomorphic granular and filled in the interspace of plagioclase, and partly chloritized. The hornblende is idiomorphic and semi-idiomorphic (Figure 3b). The Huoersen granites are flesh-red and massive-structure, and mainly composed of plagioclase (45%), quartz (35%), K-feldspar (10%), and biotite (5%) and a few accessory minerals of zircon and iron (<5%). The biotite grain occurred in the form of inclusion (Figure 3c and d). The fresh

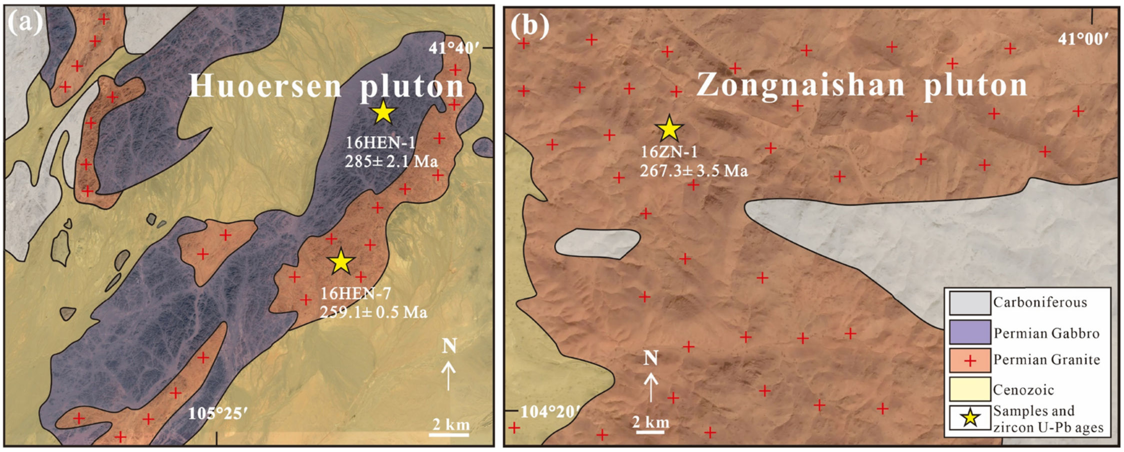

**Figure 2:** (a) Geological map of the Huoersen pluton (modified after geological map of 1:200,000). (b) Geological map of the Zongnaishan pluton (modified after geological map of 1:200,000).

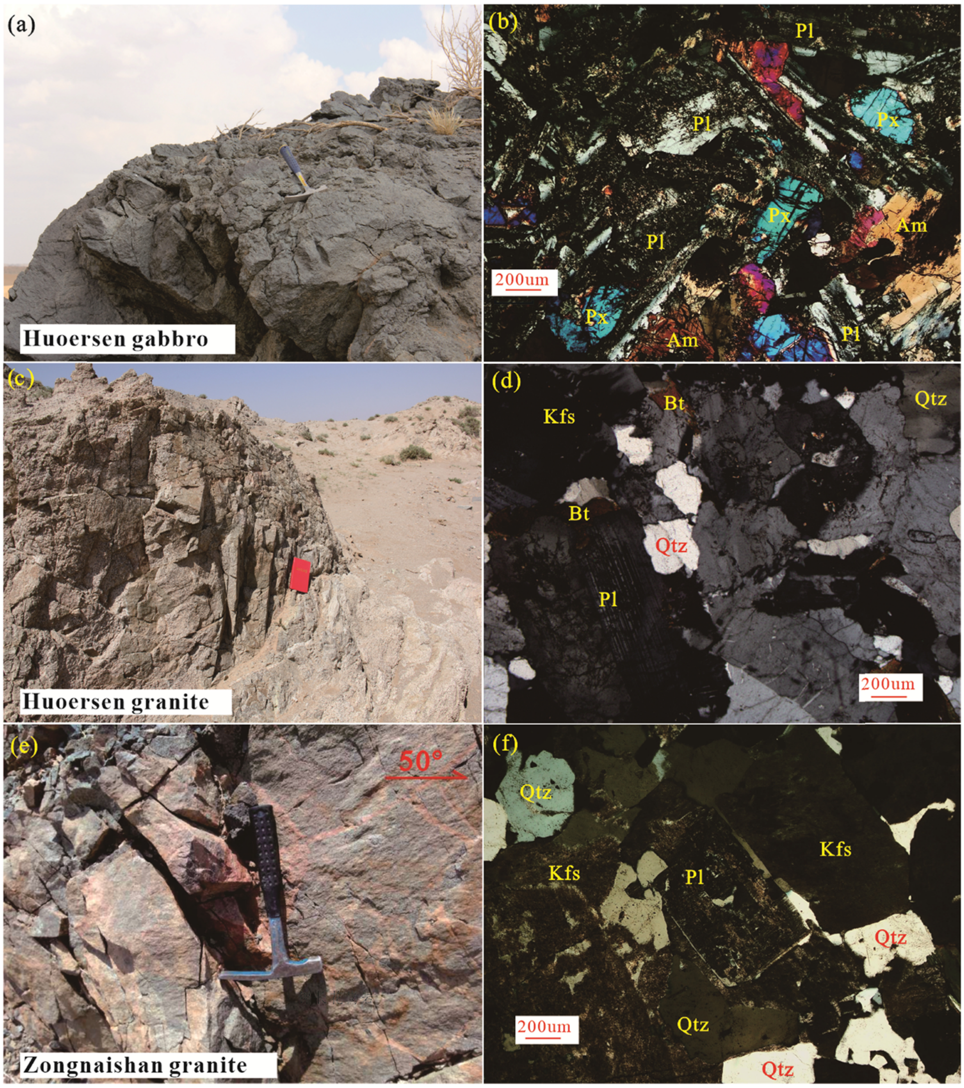

**Figure 3:** Representative field photographs and photomicrographs. (a and b) For the Huoersen gabbro. (c and d) For the Zongnaishan granite. (e and f) For the Huoersen granite. Mineral abbreviations: Qtz, quartz; Pl, plagioclase; Bt, biotite; Mus, muscovite; Am, amphibole; Kfs, K-feldspar; Px: pyroxene.

Zongnaishan granite is flesh-red (Figure 3e), with medium granitic texture and massive structure. The main mineral composition is potassium feldspar (40%), plagioclase (10%), quartz (35%), biotite (5–10%), and a small amount of amphibole (<5%) (Figure 3f).

## 4 Analytical methods

Zircon cathodoluminescence (CL) images were obtained at the Langfang Chenxin Geological Service Co., Hebei, China. U-Pb dating, whole-rock major, trace element, and Sr-Nd-Hf isotope analyses were performed at the Key Laboratory of Mineral Resources in Western China, Lanzhou University, Lanzhou, China.

### 4.1 Zircon U-Pb dating

After separation by conventional heavy liquid and magnetic techniques, zircon grains from studied samples were hand-picked and embedded in an epoxy mount under a binocular microscope and then polished to expose half of the zircon grains. The U-Pb isotope ratios of the selected zircons were measured using an Agilent 7500X inductively coupled plasma mass spectrometry (ICP-MS) instrument combined with a GeoLas200M laser ablation (LA) system. The zircon standard 91500 [40] was used as the age standard. The reference glass NIST 610 [41] and Si were applied as external and internal standards, respectively. The spot diameter was ~30 μm and the analytical techniques are referred to [42]. Data reduction was performed using the Glitter (ver. 4.0) program, and common Pb was corrected using the common lead correction program [41]. Concordia plots and weighted mean ages were generated using the Isoplot program [43]

## 4.2 Major and trace element analyses

Major element compositions were analyzed by ICP optical emission spectroscopy. The analytical accuracy was better than 2%. The loss on ignition (LOI) was obtained by heating approximately 0.5 g of dried sample powder at 1,000°C for 2 h. Trace element contents were analyzed by ICP-MS on an Agilent 7700X instrument, and the analytical errors were less than 10%. The US Geological Survey reference materials AGV-2 and BCR-2 were used as standards.

## 4.3 Whole-rock Sr-Nd-Hf isotopic

The rock samples' powders were mixed with 0.5 ml 60 wt% $HNO_3$ and 1.0 ml 40 wt% HF in high-pressure PTFE bombs. These bombs were steel-jacketed and placed in the oven at 195°C for 3 days for digestion. The digested samples were then dried on a hotplate at 150°C for 2 h and reconstituted in 1.5 ml of 1.5 N HCl before ion exchange purification. The analytical procedure was the same as that described by [44]. The diluted solution was introduced into a Nu Instruments Nu Plasma II MC-ICP-MS (Wrexham, Wales, UK) through a Teledyne Cetac Technologies Aridus II desolating nebulizer system (Omaha, Nebraska, USA). Raw data of isotopic ratios were internally corrected for mass fractionation by normalizing to $^{86}Sr/^{88}Sr = 0.1194$, $^{146}Nd/^{144}Nd = 0.7219$ for Nd, and $^{179}Hf/^{177}Hf = 0.7325$ for Hf with exponential law. International isotopic standards (NIST SRM 987 for Sr, JNdi-1 for Nd, Alfa Hf) were periodically analyzed to correct instrumental drift. Geochemical reference materials of USGS BCR-2, BHVO-2, AVG-2, and RGM-2 were treated as quality control.

# 5 Results

## 5.1 Zircon U-Pb age

The LA-ICP-MS zircon dating results of Huoersen granite, Huoersen gabbro, and Zongnaishan granite from the Alxa region are given in Table 1.

### 5.1.1 Huoersen gabbro

The zircons from the Huoersen gabbro are 100–150 μm long euhedral, in which ratios of length to width vary from 1:1 to 1:2. The CL image of zircons has obvious concentric oscillatory zoning (Figure 4a) and high Th/U ratios (0.28–2.16), indicating a magmatic origin [44]. The nine zircons from Huoersen gabbro were analyzed for U-Pb ages, with a $^{206}Pb/^{238}U$ weighted mean age of 285.0 ± 2.1 Ma (mean square of weighted deviates [MSWD] = 0.24) (Figure 4a).

### 5.1.2 Zongnaishan granite

The zircons from Zonnaishan granites show subhedral granular with sizes ranging from 50 to 70 μm and have dark bands in the CL image (Figure 4b). Seventeen zircons for Zongnaishan granite were analyzed. The Th/U ratios from 0.22 to 2.65 indicate the characteristics of magmatic zircons [45]. Seventeen zircon ages ranged from 259 ± 6 to 277 ± 8 Ma, with a weighted mean age of 267.3 ± 3.5 Ma (MSWD = 1.9) (Figure 4b).

### 5.1.3 Huoersen granite

The zircon from the Huoersen granites shows euhedral to subhedral with sizes ranging from 50 to 150 μm and has oscillatory zoning in the CL image (Figure 4c). Twenty zircons for granite were analyzed. They have high Th/U ratios (0.36–0.68), which are characteristics of magmatic zircons [45]. Nineteen zircon analyses yielded concordant $^{206}Pb/^{238}U$ ages ranging from 257 ± 3 to 265 ± 3 Ma, $^{207}Pb/^{235}U$ ages ranging from 256 ± 3 to 264 ± 4 Ma, with a concordant $^{206}Pb/^{238}U$ age of 259.1 ± 0.51 Ma (MSWD = 0.091) (Figure 4c).

## 5.2 Whole-rock major and trace element composition

Whole-rock major and trace element compositions of all samples from Huoersen granite and gabbro and Zongnaishan granite are given in Table 2.

### 5.2.1 Huoersen gabbro

The samples of Huoersen gabbro have low-to-moderate LOL (1.32–1.83%). They show high CaO (9.9–12.7 wt%), MgO (7.0–8.6 wt%), and $TiO_2$ (1.8–2.0 wt%), low $SiO_2$

**Table 1:** Zircon LA-ICP-MS U-Pb isotopic data of the Huoersen and Zongnaishan pluton in the southern Alxa region

| Spot no. | Isotopic ratios | | | | Ages (Ma) | | | |
|---|---|---|---|---|---|---|---|---|
| | $^{207}Pb/^{235}U$ | | $^{206}Pb/^{238}U$ | | $^{207}Pb/^{235}U$ | | $^{206}Pb/^{238}U$ | |
| | Ratios | ±1σ | Ratios | ±1σ | Age | ±1σ | Age | ±1σ |
| **Huoersen gabbro** | | | | | | | | |
| 16HEN1-1 | 0.33537 | 0.00414 | 0.04505 | 0.00056 | 294 | 3 | 284 | 3 |
| 16HEN1-2 | 0.34448 | 0.00698 | 0.04534 | 0.00058 | 301 | 5 | 286 | 4 |
| 16HEN1-3 | 0.30928 | 0.00395 | 0.04548 | 0.00056 | 274 | 3 | 287 | 3 |
| 16HEN1-4 | 0.33601 | 0.0044 | 0.04489 | 0.00055 | 294 | 3 | 283 | 3 |
| 16HEN1-5 | 0.32553 | 0.00833 | 0.04505 | 0.00058 | 286 | 6 | 284 | 4 |
| 16HEN1-6 | 0.33971 | 0.00761 | 0.04544 | 0.00056 | 297 | 6 | 286 | 3 |
| 16HEN1-7 | 0.31949 | 0.00709 | 0.04495 | 0.00056 | 282 | 5 | 283 | 3 |
| 16HEN1-8 | 0.34199 | 0.00398 | 0.04539 | 0.00052 | 299 | 3 | 286 | 3 |
| 16HEN1-9 | 0.30707 | 0.0058 | 0.04544 | 0.00053 | 272 | 5 | 286 | 3 |
| **Zongnaishan granite** | | | | | | | | |
| 16ZN1-1 | 0.31475 | 0.01218 | 0.04104 | 0.00106 | 278 | 10 | 259 | 6 |
| 16ZN1-2 | 0.29263 | 0.01258 | 0.04225 | 0.00112 | 261 | 10 | 267 | 6 |
| 16ZN1-3 | 0.30369 | 0.0133 | 0.04267 | 0.00114 | 269 | 10 | 269 | 8 |
| 16ZN1-4 | 0.31630 | 0.01188 | 0.04260 | 0.00112 | 279 | 10 | 269 | 6 |
| 16ZN1-5 | 0.31847 | 0.01432 | 0.04309 | 0.00118 | 281 | 12 | 272 | 8 |
| 16ZN1-6 | 0.30383 | 0.01082 | 0.04204 | 0.0011 | 269 | 8 | 265 | 6 |
| 16ZN1-7 | 0.32037 | 0.0146 | 0.04278 | 0.00118 | 282 | 12 | 270 | 8 |
| 16ZN1-8 | 0.29858 | 0.0124 | 0.04129 | 0.00112 | 265 | 10 | 261 | 6 |
| 16ZN1-9 | 0.31734 | 0.0131 | 0.04398 | 0.00120 | 280 | 10 | 277 | 8 |
| 16ZN1-10 | 0.33119 | 0.01528 | 0.04213 | 0.00120 | 290 | 12 | 266 | 8 |
| 16ZN1-11 | 0.32052 | 0.0137 | 0.04364 | 0.00120 | 282 | 10 | 275 | 8 |
| 16ZN1-12 | 0.33054 | 0.01488 | 0.04303 | 0.00118 | 290 | 12 | 272 | 8 |
| 16ZN1-13 | 0.31241 | 0.01442 | 0.04228 | 0.00118 | 276 | 12 | 267 | 8 |
| 16ZN1-14 | 0.31095 | 0.0132 | 0.04254 | 0.00114 | 275 | 10 | 269 | 8 |
| 16ZN1-15 | 0.29175 | 0.01294 | 0.04144 | 0.00112 | 260 | 10 | 262 | 6 |
| 16ZN1-16 | 0.31947 | 0.01336 | 0.04283 | 0.00114 | 281 | 10 | 270 | 8 |
| 16ZN1-17 | 0.30283 | 0.01292 | 0.04274 | 0.00114 | 269 | 10 | 270 | 8 |
| **Huoersen granite** | | | | | | | | |
| 16HEN7-1 | 0.29175 | 0.00513 | 0.04173 | 0.00046 | 260 | 4 | 264 | 3 |
| 16HEN7-2 | 0.29309 | 0.00469 | 0.0411 | 0.00045 | 261 | 4 | 260 | 3 |
| 16HEN7-3 | 0.28699 | 0.00623 | 0.0408 | 0.00046 | 256 | 5 | 258 | 3 |
| 16HEN7-4 | 0.29099 | 0.00395 | 0.04097 | 0.00045 | 259 | 3 | 259 | 3 |
| 16HEN7-5 | 0.29202 | 0.00389 | 0.04087 | 0.00044 | 260 | 3 | 258 | 3 |
| 16HEN7-6 | 0.29011 | 0.0058 | 0.04083 | 0.00046 | 259 | 5 | 258 | 3 |
| 16HEN7-7 | 0.28892 | 0.00725 | 0.04092 | 0.00048 | 258 | 6 | 259 | 3 |
| 16HEN7-8 | 0.2923 | 0.00387 | 0.04074 | 0.00044 | 260 | 3 | 257 | 3 |
| 16HEN7-9 | 0.29053 | 0.00414 | 0.04121 | 0.00045 | 259 | 3 | 260 | 3 |
| 16HEN7-10 | 0.29147 | 0.00442 | 0.04101 | 0.00045 | 260 | 3 | 259 | 3 |
| 16HEN7-11 | 0.29047 | 0.00385 | 0.04071 | 0.00044 | 259 | 3 | 257 | 3 |
| 16HEN7-12 | 0.28973 | 0.00414 | 0.0406 | 0.00044 | 258 | 3 | 257 | 3 |
| 16HEN7-13 | 0.29017 | 0.00391 | 0.04058 | 0.00044 | 259 | 3 | 256 | 3 |
| 16HEN7-14 | 0.29157 | 0.00445 | 0.04091 | 0.00045 | 260 | 3 | 258 | 3 |
| 16HEN7-15 | 0.28985 | 0.00382 | 0.04094 | 0.00045 | 258 | 3 | 259 | 3 |
| 16HEN7-16 | 0.29205 | 0.00519 | 0.04161 | 0.00046 | 260 | 4 | 263 | 3 |
| 16HEN7-17 | 0.29679 | 0.00528 | 0.04189 | 0.00047 | 264 | 4 | 265 | 3 |
| 16HEN7-18 | 0.29331 | 0.00394 | 0.04132 | 0.00045 | 261 | 3 | 261 | 3 |
| 16HEN7-19 | 0.2898 | 0.00376 | 0.04101 | 0.00045 | 258 | 3 | 259 | 3 |

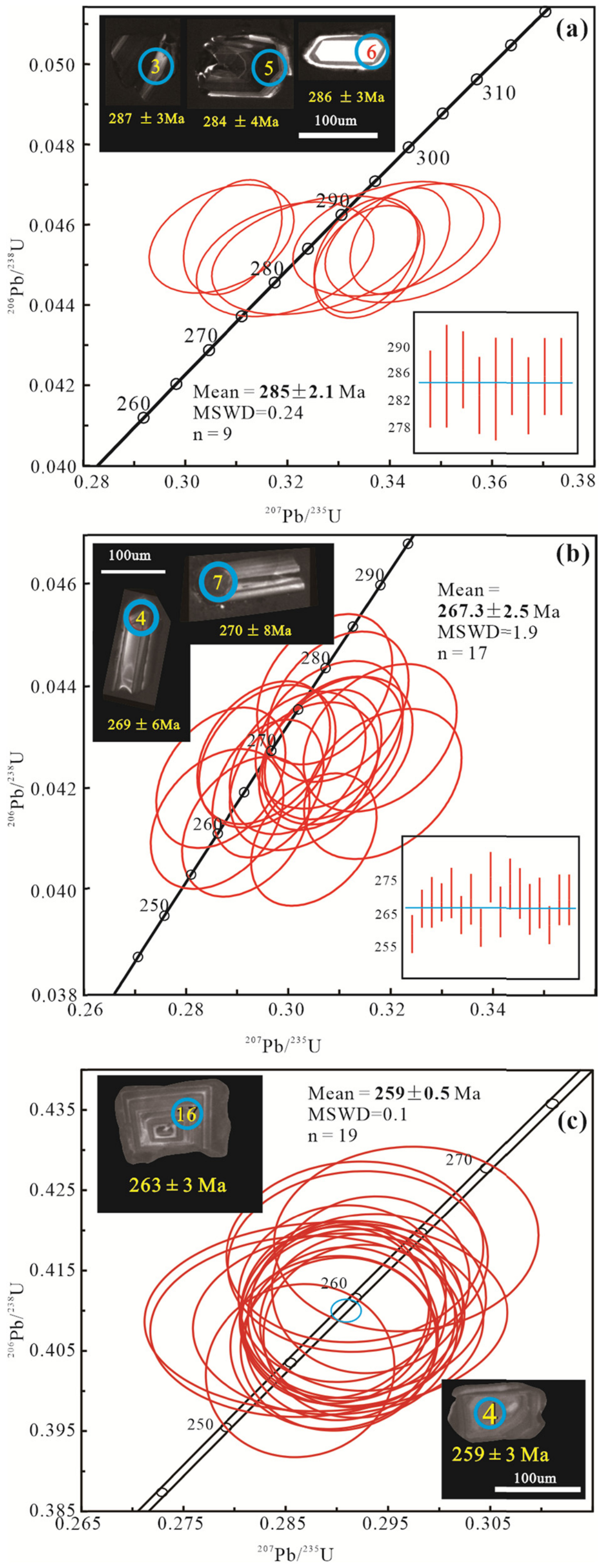

**Figure 4:** Representative CL images and zircon U–Pb concordia diagram for the samples from the southern Alxa region. (a) Huoersen gabbro. (b) Zongnaishan granite. (c) Huoersen granite.

(45.7–48.3 wt%), $Al_2O_3$ (14.4–16.5 wt%), and $K_2O$ (1.2–2.0 wt%) contents, and relatively high $Na_2O$ (3.4–4.5 wt%), with low $K_2O/Na_2O$ ratios (0.3–0.6). In the TAS diagram (Figure 5a), samples are plotted into in the field of monzogabbro. In the $SiO_2$-$K_2O$ diagram (Figure 5b), most samples plot into the shoshonitic series.

The samples of Huoersen gabbro have high rare earth element (REE) (435–535 ppm). In the chondrite normalized REE diagram (Figure 6a), samples show higher light REE (LREE) and relatively lower heavy REE (HREE), with $(La/Yb)_N$ ratios of 32.81–51.63. In the primitive mantle-normalized spider diagram (Figure 6b), the samples exhibit enrichments in LILEs (e.g., Rb, Sr, Ba), weakly enrichments in Zr-Hf, and depletions in HFSEs (e.g., Nb, Ta, Ti).

### 5.2.2 Zongnaishan granite

The samples of Zongnaishan granites have moderate $SiO_2$ (67.3–69.9%), $Al_2O_3$ (15.7–16.2%), $Na_2O$ (3.8–4.0%), and $K_2O$ (4.4–4.7%) contents, and the ratios of $K_2O/Na_2O$ are 1.1–1.2. The samples plot into the field of quartz monzonite in the TAS diagram (Figure 5a) and belong to the high-K calc-alkaline series in the $K_2O$-$SiO_2$ diagram (Figure 5b). The samples have low $TiO_2$ (0.30–0.39 wt%), CaO (1.52–2.07 wt%), and MgO (0.54–0.61 wt%) contents, and Mg number [Mg# = $Mg/(Mg + Fe^{2+})$] values are 27–32. In the A/NK-A/CNK diagram (Figure 5c), the samples' plot belongs to the peraluminous series.

The REE of samples varies from 144 to 329 ppm. In the chondrite normalized REE diagram (Figure 6c), the samples are characterized by moderate negative Eu anomaly with δEu values of 0.30–0.49. In the primitive mantle-normalized spider diagram (Figure 6d), the samples exhibit enrichments in Rb, Th, U, and K and depletions in Nb, Ta, Sr, P, and Ti.

### 5.2.3 Huoersen granite

The samples of Huoersen granite exhibit extreme high $SiO_2$ (74.78-77.44 wt%) contents, low $TiO_2$ (0.18–0.22 wt%), $Al_2O_3$ (11.61–12.35 wt%), MgO (0.13–0.22 wt%), $P_2O_5$ (0.01–0.05 wt%), and CaO (0.23–0.70 wt%) contents, with Mg# values ranging from 45 to 63. The $Na_2O$ and $K_2O$ contents of 3.46–4.04 wt% and 4.52–5.72 wt%, respectively. All samples spot fall in the granite field in the TAS diagram (Figure 5a) and belong to high K-cala alkaline and shoshonite series in the $SiO_2$ vs $K_2O$ diagram (Figure 5b). In addition, they display characteristics of peralkaline series in the A/NK vs A/CNK diagram (Figure 5c).

**Table 2:** Whole-rock major (wt%) and trace element (ppm) analyses of samples from the Huoersen and Zongnaishan plutons

| Rock type | Huoersen gabbro | | | | | | Zongnaishan granite | | | | | | Huoersen granite | | | | | | |
|---|---|---|---|---|---|---|---|---|---|---|---|---|---|---|---|---|---|---|---|
| **Samples** | **16HE-1** | **16HE-2** | **16HE-3** | **16HE-4** | **16HE-5** | **16HE-6** | **16HE-7** | **16HE-8** | **16HE-9** | **16HE-10** | **16HE-11** | **16HE-12** | **16ZN-1** | **16ZN-2** | **16ZN-3** | **16ZN-4** | **16ZN-5** | **16ZN-6** | **16ZN-7** |
| $SiO_2$ | 47.66 | 48.31 | 46.82 | 47.74 | 45.73 | 45.88 | 67.32 | 67.91 | 68.00 | 68.23 | 69.87 | 67.98 | 75.13 | 75.31 | 74.78 | 74.86 | 77.44 | 75.97 | 75.82 |
| $TiO_2$ | 1.90 | 1.91 | 2.00 | 1.76 | 1.84 | 1.87 | 15.73 | 16.04 | 16.18 | 15.99 | 15.83 | 15.72 | 0.20 | 0.21 | 0.18 | 0.18 | 0.19 | 0.18 | 0.19 |
| $Al_2O_3$ | 14.39 | 15.43 | 14.64 | 16.50 | 16.01 | 16.06 | 0.38 | 0.39 | 0.33 | 0.30 | 0.36 | 0.32 | 12.35 | 12.25 | 11.84 | 12.22 | 11.61 | 12.01 | 11.82 |
| $Fe_2O_3$ | 8.71 | 8.47 | 8.92 | 7.94 | 9.18 | 8.71 | 3.15 | 2.93 | 2.63 | 2.56 | 2.82 | 2.87 | 1.71 | 1.66 | 1.60 | 1.41 | 1.59 | 1.36 | 1.72 |
| MgO | 8.62 | 7.11 | 7.36 | 7.05 | 6.96 | 7.65 | 0.06 | 0.05 | 0.05 | 0.05 | 0.05 | 0.06 | 0.22 | 0.17 | 0.17 | 0.15 | 0.19 | 0.13 | 0.17 |
| BaO | 0.14 | 0.13 | 0.12 | 0.14 | 0.11 | 0.14 | 0.60 | 0.59 | 0.61 | 0.61 | 0.55 | 0.54 | 0.02 | 0.02 | 0.01 | 0.01 | 0.01 | 0.01 | 0.01 |
| CaO | 10.96 | 10.76 | 11.54 | 9.86 | 12.74 | 11.11 | 2.07 | 1.60 | 1.63 | 1.60 | 1.52 | 1.96 | 0.23 | 0.63 | 0.61 | 0.70 | 0.61 | 0.62 | 0.52 |
| $Na_2O$ | 3.39 | 3.47 | 3.42 | 4.50 | 4.06 | 3.90 | 3.86 | 3.91 | 4.03 | 4.01 | 3.88 | 3.78 | 4.04 | 3.96 | 3.78 | 3.94 | 3.46 | 3.82 | 3.81 |
| $K_2O$ | 1.96 | 1.60 | 1.53 | 1.91 | 1.19 | 2.03 | 4.45 | 4.38 | 4.66 | 4.50 | 4.47 | 4.54 | 5.57 | 5.55 | 5.42 | 5.72 | 4.52 | 5.39 | 5.41 |
| $P_2O_5$ | 1.59 | 1.36 | 1.63 | 1.53 | 1.82 | 1.54 | 0.14 | 0.11 | 0.17 | 0.10 | 0.09 | 0.10 | 0.05 | 0.03 | 0.01 | 0.02 | 0.02 | 0.03 | 0.05 |
| LOI | 1.32 | 1.75 | 1.60 | 1.83 | 1.60 | 1.68 | 1.51 | 0.95 | 0.76 | 0.91 | 0.87 | 1.36 | 0.61 | 0.70 | 0.68 | 0.71 | 0.98 | 0.74 | 0.89 |
| Total | 100.63 | 100.30 | 99.57 | 100.78 | 101.24 | 100.58 | 99.27 | 98.86 | 99.05 | 98.86 | 100.31 | 99.23 | 100.12 | 100.47 | 99.09 | 99.92 | 100.61 | 100.27 | 100.42 |
| Mg# | 63.81 | 59.94 | 59.55 | 61.29 | 57.46 | 61.02 | 27.44 | 28.56 | 31.53 | 32.11 | 27.91 | 27.20 | 18.33 | 15.49 | 16.02 | 15.83 | 17.58 | 14.24 | 14.64 |
| La | 107 | 79.74 | 89.57 | 127 | 126 | 89.29 | 50.70 | 67.60 | 27.20 | 28.70 | 54.90 | 45.20 | 53.99 | 54.73 | 45.85 | 44.19 | 49.25 | 45.30 | 52.00 |
| Ce | 186 | 185 | 213 | 219 | 204 | 200 | 109 | 140 | 55.90 | 58.50 | 113.50 | 95.70 | 108 | 112 | 101 | 90.04 | 108 | 101 | 107 |
| Pr | 23.98 | 24.05 | 28.11 | 27.48 | 25.14 | 25.43 | 12.75 | 16.05 | 6.39 | 6.88 | 12.95 | 11.05 | 13.61 | 14.01 | 11.72 | 11.24 | 12.54 | 11.76 | 13.12 |
| Nd | 101 | 101 | 118 | 112 | 104 | 105 | 48.20 | 59.40 | 24.10 | 26.30 | 48.20 | 42.00 | 51.30 | 53.12 | 44.25 | 42.52 | 47.51 | 44.49 | 49.65 |
| Sm | 16.71 | 16.69 | 19.75 | 17.83 | 16.93 | 17.34 | 9.44 | 11.05 | 4.95 | 5.44 | 9.14 | 8.14 | 10.42 | 10.89 | 9.16 | 8.80 | 9.68 | 9.23 | 10.06 |
| Eu | 4.16 | 4.29 | 4.78 | 4.32 | 4.26 | 4.31 | 0.77 | 0.92 | 0.72 | 0.73 | 0.88 | 0.86 | 0.55 | 0.56 | 0.51 | 0.47 | 0.54 | 0.51 | 0.52 |
| Gd | 10.96 | 10.72 | 12.54 | 11.29 | 10.84 | 10.82 | 6.67 | 7.98 | 4.04 | 4.07 | 6.57 | 5.88 | 9.72 | 10.26 | 8.76 | 8.32 | 8.92 | 8.47 | 9.20 |
| Tb | 1.22 | 1.22 | 1.37 | 1.29 | 1.20 | 1.21 | 0.83 | 0.93 | 0.54 | 0.53 | 0.81 | 0.71 | 1.62 | 1.73 | 1.49 | 1.41 | 1.51 | 1.42 | 1.56 |
| Dy | 5.78 | 5.57 | 6.37 | 5.92 | 5.62 | 5.63 | 3.91 | 4.32 | 2.91 | 2.69 | 3.78 | 3.23 | 10.17 | 11.03 | 9.41 | 8.97 | 9.37 | 9.04 | 9.74 |
| Ho | 0.96 | 0.91 | 1.06 | 0.97 | 0.90 | 0.94 | 0.60 | 0.65 | 0.50 | 0.44 | 0.59 | 0.47 | 2.08 | 2.26 | 1.95 | 1.84 | 1.90 | 1.84 | 1.98 |
| Er | 2.44 | 2.34 | 2.64 | 2.52 | 2.42 | 2.39 | 1.33 | 1.48 | 1.32 | 1.07 | 1.32 | 1.06 | 6.17 | 6.80 | 5.95 | 5.64 | 5.77 | 5.62 | 6.05 |
| Tm | 0.29 | 0.28 | 0.32 | 0.32 | 0.29 | 0.29 | 0.17 | 0.18 | 0.19 | 0.16 | 0.16 | 0.13 | 0.86 | 0.99 | 0.87 | 0.81 | 0.82 | 0.83 | 0.89 |
| Yb | 1.77 | 1.71 | 1.96 | 1.91 | 1.76 | 1.78 | 1.05 | 1.07 | 1.22 | 0.99 | 1.04 | 0.82 | 5.70 | 6.62 | 5.69 | 5.34 | 5.68 | 5.69 | 6.02 |
| Lu | 0.26 | 0.24 | 0.28 | 0.29 | 0.26 | 0.26 | 0.15 | 0.16 | 0.18 | 0.15 | 0.15 | 0.12 | 0.84 | 0.97 | 0.85 | 0.80 | 0.84 | 0.85 | 0.87 |
| ΣREE | 464 | 434 | 501 | 534 | 504 | 465 | 261 | 329 | 144 | 148 | 269 | 227 | 275 | 286 | 247 | 230 | 262 | 246 | 269 |
| LREE | 440 | 411 | 474 | 510 | 481 | 442 | 231 | 295 | 119 | 126 | 239 | 202 | 238 | 246 | 212 | 197 | 227 | 212 | 233 |
| HREE | 23.69 | 22.99 | 26.52 | 24.51 | 23.28 | 23.33 | 30.41 | 34.07 | 25.10 | 22.30 | 30.02 | 24.62 | 37.15 | 40.66 | 34.97 | 33.13 | 34.80 | 33.76 | 36.30 |
| LREE/HREE | 18.59 | 17.91 | 17.90 | 20.81 | 20.66 | 18.98 | 7.61 | 8.66 | 4.75 | 5.67 | 7.98 | 8.24 | 6.43 | 6.05 | 6.09 | 5.95 | 6.54 | 6.31 | 6.43 |
| δEu | 0.88 | 0.92 | 0.87 | 0.87 | 0.90 | 0.90 | 0.30 | 0.30 | 0.49 | 0.47 | 0.35 | 0.38 | 0.17 | 0.16 | 0.17 | 0.17 | 0.17 | 0.17 | 0.16 |
| δCe | 0.86 | 1.03 | 1.04 | 0.87 | 0.84 | 1.02 | 0.92 | 0.92 | 0.91 | 0.91 | 0.92 | 0.92 | 0.96 | 0.97 | 1.05 | 0.97 | 1.04 | 1.05 | 0.99 |
| Rb | 164 | 104 | 98.14 | 109 | 62.77 | 112 | 185 | 179 | 197 | 168 | 183 | 168 | 184 | 201 | 198 | 213 | 193 | 210 | 198 |
| Ba | 1,785 | 1,203 | 1,170 | 1,710 | 953 | 1,258 | 780 | 780 | 640 | 660 | 790 | 770 | 141 | 141 | 124 | 123 | 132 | 123 | 125 |
| Th | 8.28 | 10.84 | 10.60 | 15.08 | 11.94 | 10.13 | 24.30 | 32.70 | 16.90 | 21.40 | 25.00 | 19.75 | 20.31 | 22.14 | 19.49 | 18.28 | 19.92 | 20.88 | 21.26 |
| U | 1.63 | 2.22 | 2.06 | 3.01 | 2.20 | 2.04 | 1.70 | 2.30 | 1.60 | 1.40 | 1.90 | 1.40 | 2.85 | 3.53 | 3.20 | 2.92 | 3.54 | 3.04 | 3.03 |
| Ta | 0.51 | 0.32 | 0.38 | 0.40 | 0.28 | 0.34 | 1.45 | 1.41 | 2.46 | 1.24 | 1.30 | 0.94 | 1.27 | 1.43 | 1.18 | 1.23 | 1.21 | 1.23 | 1.43 |

*(Continued)*

**Table 2:** *Continued*

| Rock type | Huoersen gabbro | | | | | | Zongnaishan granite | | | | | | Huoersen granite | | | | | | |
|---|---|---|---|---|---|---|---|---|---|---|---|---|---|---|---|---|---|---|---|
| **Samples** | **16HE-1** | **16HE-2** | **16HE-3** | **16HE-4** | **16HE-5** | **16HE-6** | **16HE-7** | **16HE-8** | **16HE-9** | **16HE-10** | **16HE-11** | **16HE-12** | **16ZN-1** | **16ZN-2** | **16ZN-3** | **16ZN-4** | **16ZN-5** | **16ZN-6** | **16ZN-7** |
| Nb | 9.90 | 7.37 | 8.59 | 9.38 | 7.22 | 8.00 | 14.90 | 13.70 | 13.60 | 10.50 | 12.90 | 12.00 | 20.65 | 21.76 | 18.21 | 18.66 | 19.14 | 17.92 | 21.18 |
| Sr | 2,355 | 3,016 | 3,162 | 3,305 | 4,703 | 3,004 | 228 | 267 | 268 | 260 | 252 | 237 | 30.82 | 33.33 | 27.30 | 23.06 | 34.73 | 21.19 | 27.60 |
| P | 6,940 | 5,939 | 7,132 | 6,672 | 7,951 | 6,879 | 611 | 480 | 742 | 436 | 393 | 436 | 226 | 122 | 42.74 | 104 | 80.76 | 153 | 225 |
| Zr | 205 | 232 | 227 | 350 | 210 | 219 | 98.20 | 93.40 | 79.40 | 72.30 | 88.40 | 88.70 | 273 | 287 | 312.56 | 248 | 235 | 205 | 203 |
| Hf | 5.16 | 5.37 | 5.32 | 6.25 | 4.86 | 5.33 | 3.70 | 3.60 | 3.00 | 2.70 | 3.40 | 3.40 | 7.45 | 8.04 | 8.11 | 7.74 | 7.50 | 7.23 | 7.17 |
| Y | 24.29 | 23.57 | 27.19 | 25.63 | 24.40 | 24.17 | 15.70 | 17.30 | 14.20 | 12.20 | 15.60 | 12.20 | 56.24 | 62.74 | 54.24 | 51.41 | 51.97 | 49.47 | 54.10 |

These granite samples have high REE contents (230–280 ppm). In the chondrite-normalized REE diagrams (Figure 6e), the granite shows enriched LREE, with middle negative Eu anomalies (Eu/Eu* = 0.16−0.17). In the primitive mantle-normalized trace element diagrams (Figure 6f), all granites sample depletions in Ba, Nb, Ta, Sr, P, and Ti, and enrichments in Rb, Th, U, P, K, and Pb.

## 5.3 Whole-rock Sr-Nd-Hf isotopic

Whole-rock Sm-Nd and Lu-Hf isotopic data for the Huoersen gabbro and granite in the Alxa region are given in Table 3. Whole-rock Rb-Sr and Sm-Nd isotopic data for the Zongnaishan granite in the Alxa region are given in Table 4. The initial $^{87}Sr/^{86}Sr$, $^{143}Nd/^{144}Nd$, $^{176}Hf/^{177}Hf$, and $\varepsilon_{Nd}(t)$ and $\varepsilon_{Hf}(t)$ values were calculated by using the ages of zircon U-Pb for all samples.

### 5.3.1 Huoersen gabbro

The samples from Huoersen gabbro have initial $^{143}Nd/^{144}Nd$ ratios of 0.512372–0.512383 and positive $\varepsilon_{Nd}(t = 285\,Ma)$ values of +2.1 to +2.3. They show high initial $^{176}Hf/^{177}Hf$ values of 0.282847–0.282896 and positive $\varepsilon_{Hf}(t)$ values of +9.0 to +10.7, yielding two-stage Hf model ages of 832–791 Ma.

### 5.3.2 Zongnaishan granite

The Zongnaishan gabbro have low initial $^{87}Sr/^{86}Sr$ values of 0.707527–0.708414. They show initial $^{143}Nd/^{144}Nd$ values of 0.512191–0.510041 and negative $\varepsilon_{Nd}(t)$ values of −0.37 to −0.43, yielding two-stage Nd model ages of 1.58–1.43 Ga.

### 5.3.3 Huoersen granite

The Huoersen granites have $^{143}Nd/^{144}Nd$ ratios of 0.512579–0.512588 and $^{176}Hf/^{177}Hf$ ratios of 0.282886–0.282900. Their initial $^{143}Nd/^{144}Nd$ and $^{176}Hf/^{177}Hf$ values vary from 0.512366 to 0.512378, 0.282811 to 20.282900, respectively, and positive $\varepsilon_{Nd}(t)$ values of +1.2 to +1.5 and $\varepsilon_{Hf}(t)$ values of +7.1 to +7.7, yielding two-stage Hf model ages of 733–622 Ma.

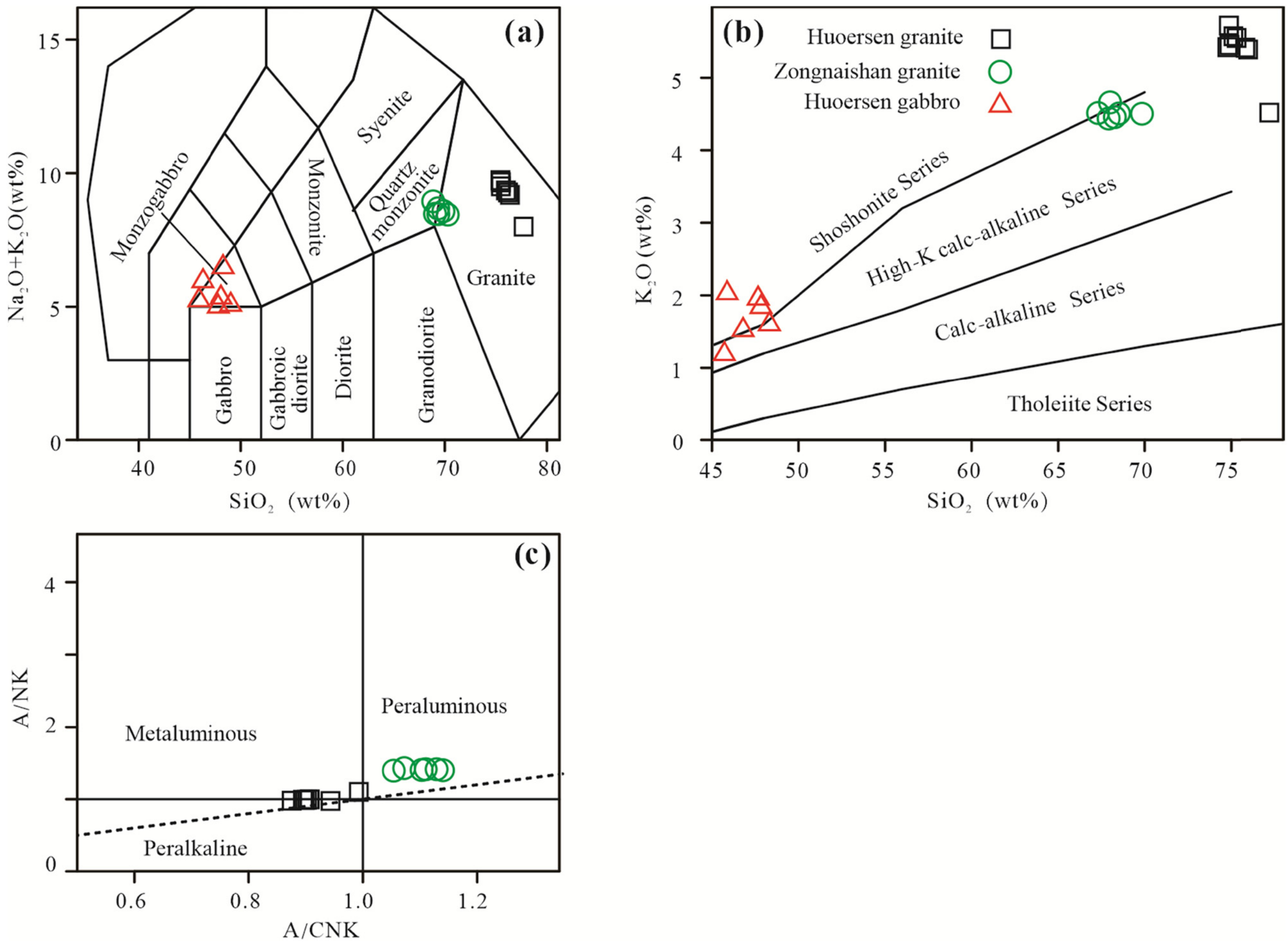

**Figure 5:** (a) Total alkali vs silica diagram [72], (b) $K_2O$ vs $SiO_2$ diagram [73], and c A/NK vs A/CNK diagram [74].

# 6 Discussion

## 6.1 Petrogenesis

### 6.1.1 Huoersen gabbro

The samples from Huoersen gabbro exhibit high MgO (6.96–8.62 wt%) contents, and varied greatly Mg# values (45–63) lower than values of primary magma (68–75) [46]. The contents of Cr (26–198 ppm) and Ni (169–223 ppm) varied widely, mean the parent magma of sample underwent fractional crystallization of olivine and pyroxene. In addition, the samples display slightly negative Eu anomalies (Figure 6a) and enrichment in Sr, suggesting that the fractional crystallization of plagioclase is weak.

The calc-alkaline Huoersen gabbro shows the characteristics of the island arc in the primitive-mantle-normalized trace element variation diagrams (Figure 6b), such as depleted in HFSEs (e.g., Nb, Ta, Ti) and enrichments in LREE and LILEs [47,48]. Remarkably, the Nb-Ta depletion could be induced by the crustal contamination of the basic magma [49]. But there is no clear contaminate signal of crustal materials for the samples from Huoersen gabbro: (a) the sample displays weakly negative Zr-Hf anomalies (Figure 6b), (b) their U/Nb ratios are very steady and not positively correlated with $SiO_2$ contents (Figure 7), and (c) the Lu/Y (0.01), Nb/La (0.08), and Nb/Ce (0.04) are much lower than the range of continental crust values (Lu/Y of 0.16–0.18, Nb/La of 0.69, and Nb/Ce of 0.33) [50]. Furthermore, the subduction metasomatic fluids could also result in the Nb-Ta depletion, and the southern Alxa region was at a subduction of PAO tectonic setting during the early Permian [10,64,22,25]. In summary, the magmatic composition of Huoersen gabbro had not been significantly affected by crustal material involvement.

The samples from Huoersen gabbro have high La/Nb ratios (10.4–17.4), indicating that their magma sources were the product of lithospheric mantle (La/Nb ratios greater than 1.5), rather than asthenosphere mantle (La/Nb ratios less than 1.5) [51]. In addition, the sample has

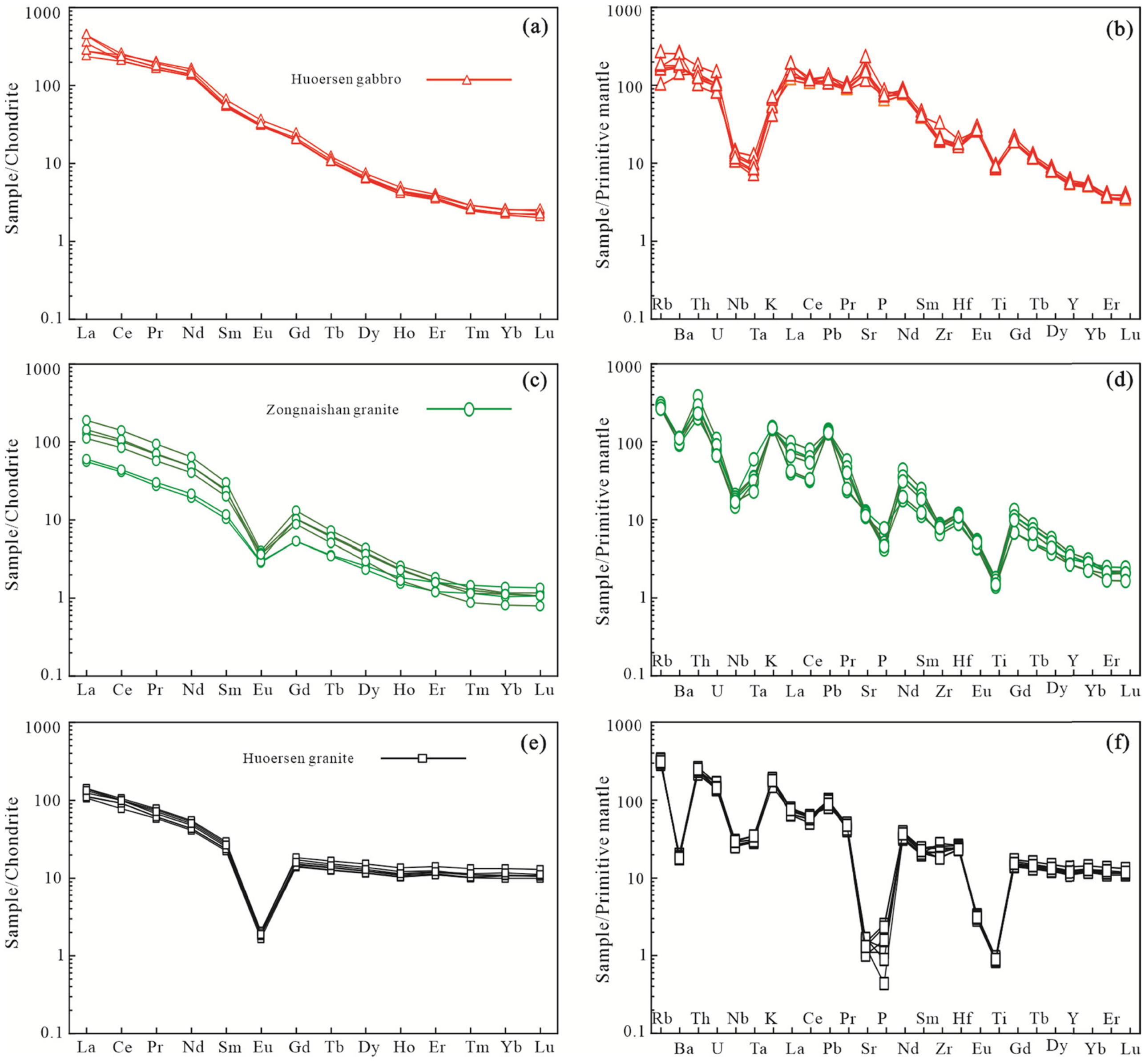

**Figure 6:** Chondrite-normalized REE patterns and primitive-mantle-normalized trace element variation diagrams. The data for chondrite and primitive mantle are from [75]. (a and b) Huoersen gabbro. (c and d) Zongnaishan granite. (e and f) Huoersen granite.

the geochemical characteristics of arc magma, reflecting the magmatic source that may be modified by subduction metasomatic fluids. The results are different from the magma of MORB (mid-ocean ridge basalt) or OIB (ocean island basalt) subjected to crustal contamination. However, the Nd-Hf isotopic systematics of Huoersen gabbro indicate that their sources are depleted mantle, which exhibit positive $\varepsilon_{\mathrm{Nd}}(t)$ (+2.1 to +2.3) and $\varepsilon_{\mathrm{Hf}}(t)$ values (+7.1 to +7.7). These decoupling characteristics of isotope and trace element are due to the metasomatism of subduction plates in the mantle source, resulting in enrichment in incompatible elements, such as K, Ba, and Sr [52]. Numerous studies have concluded that the southern CAOB occurred multistage subduction of oceanic plates during the Paleozoic [10,19,23,29,35,38]. So, the metasomatic components of the mantle source of the Huoersen gabbro parent magma are derived from the fluid released by the subduction slabs during the subduction of the PAO.

In conclusion, the Huoersen gabbro is the product of the depleted mantle metasomatized by subduction fluids.

### 6.1.2 Zongnaishan granite

Granites are important components in the continents and also closely related to collisional orogenic belt [53], which can be grouped into I-, S-, M-, and A-type granites based on

**Table 3:** Whole-rock Nd-Hf isotopic data for the Huoersen gabbro and granite

| Sample | $^{147}Sm/^{144}Nd$ | $^{143}Nd/^{144}Nd$ | $(^{143}Nd/^{144}Nd)_i$ | $2\sigma(10^{-6})$ | $\varepsilon_{Nd}(t)$ | $T_{2DM}$(Ma) | $^{176}Lu/^{177}Hf$ | $^{176}Hf/^{177}Hf$ | $(^{176}Hf/^{177}Hf)_i$ | $2\sigma(10^{-6})$ | $\varepsilon_{Hf}(t)$ | $T_{2DM}$(Ma) |
|---|---|---|---|---|---|---|---|---|---|---|---|---|
| **Huoersen gabbro** | | | | | | | | | | | | |
| 16HE-2 | 0.099240 | 0.512570 | 0.512383 | 2 | 2.30 | 869 | 0.007096 | 0.282885 | 0.282847 | 4 | 9.00 | 733 |
| 16HE-3 | 0.099280 | 0.512568 | 0.512380 | 2 | 2.20 | 873 | 0.006397 | 0.282903 | 0.282868 | 5 | 9.80 | 685 |
| 16HE-4 | 0.100390 | 0.512562 | 0.512372 | 2 | 2.10 | 887 | 0.007399 | 0.282904 | 0.282864 | 3 | 9.60 | 694 |
| 16HE-6 | 0.095360 | 0.512560 | 0.512379 | 3 | 2.20 | 875 | 0.006527 | 0.282931 | 0.282896 | 5 | 10.70 | 622 |
| **Huoersen granite** | | | | | | | | | | | | |
| 16HE-7 | 0.122757 | 0.512587 | 0.512379 | 2 | 1.45 | 912 | 0.016063 | 0.282889 | 0.282811 | 4 | 7.08 | 832 |
| 16HE-8 | 0.123930 | 0.512588 | 0.512378 | 2 | 1.43 | 914 | 0.017154 | 0.282896 | 0.282813 | 3 | 7.14 | 828 |
| 16HE-9 | 0.125140 | 0.512579 | 0.512367 | 2 | 1.22 | 931 | 0.014805 | 0.282886 | 0.282814 | 3 | 7.19 | 825 |
| 16HE-10 | 0.125061 | 0.512583 | 0.512371 | 2 | 1.30 | 925 | 0.014609 | 0.282900 | 0.282829 | 3 | 7.72 | 791 |

their geochemical characteristics and tectonic setting [54–58]. The samples from Zongnaishan granite have moderate $SiO_2$ (67.3–69.8 wt%) and $Al_2O_3$ contents (15.7–16.2 wt%). Their A/CNK values (1.05–1.14) are not exactly correspond with the characteristics of S-type granites (A/CNK value greater than 1.1) [58], and no aluminum-rich minerals (leucite, cordierite, etc.) are found in the mineral composition, so they do not belong to S-type granites. The samples have low (Zr + Nb + Ce + Y) values (154–264 ppm) and 10000Ga/Al ratios of 2.58–2.86. These are not completely consistent with the high $SiO_2$, (Zr + Nb + Ce + Y) value (greater than 350 ppm) and 10,000 Ga/Al ratios (greater than 2.6) of A-type granites [57]. All samples plot into the OTG (unfractionated I- and S-type granites) field in the (Zr + Nb + Ce + Y) − ($NaO_2$ + $K_2O$)/CaO diagram (Figure 8). Therefore, the Zongnaishan granite is in agreement with I-type granites.

The Zongnaishan granites show depleted in HFSEs (e.g., Nb, Ta, Zr, and Ti), and enrichment in LILEs (e.g., Rb and Th), indicating that the magma source is dominated by components of continental crust. The samples' enrichment in K and depletion of P also reflect the magma derived from crust. Moreover, the samples from Zongnaishan have initial $^{87}Sr/^{86}Sr$ values of 0.707527–0.708414, and negative $\varepsilon_{Nd}(t)$ values (−0.37 to −0.43) and two-stage Nd model ages of 1.58–1.43 Ga, suggesting that the Zongnaoshan granite is the product of remelting Neoproterozoic crust.

### 6.1.3 Huoersen granite

The samples from Huoersen granite have high $SiO_2$, $K_2O$, and $Na_2O$ contents, low MgO and CaO contents, enrichment in Rb, Th, U, Zr, and Hf, and depleted in Ba, Sr, Ti, Nb, and Ta, with 10,000 Ga/Al ratios of 4.2 (Zr + Nb + Ce + Y), values of 375–486 ppm, and are peralkaline (Figure 4a, A/CNK < 1), similar to that of A-type granites [54,56,57]. Moreover, all samples spot into the field of A-type granites in the (Zr + Nb + Ce + Y) − ($NaO_2$ + $K_2O$)/CaO diagram (Figure 8). Therefore, the Huoersen granite belongs to A-type granites.

Previous studies proposed various petrogenetic models for A-type granites: (a) fractional crystallization of mantle basaltic magma [59]; (b) partial melting of lower crustal material [57]; and (c) mixing of mantle magmas with crustal material [60]. It is usually accompanied by lots of mafic-ultramafic magmatism if A-type granite is derived from the crystallization differentiation of partially melted basalt magma [60], such as alkali granites in the western CAOB [53,61]. But there are no additional mafic magmas in the Alxa area. The sample has positive $\varepsilon_{Nd}(t)$ (+1.2 to +1.5) and $\varepsilon_{Hf}(t)$ values (+7.1 to +7.7), and $T_{2DM}$ of 832–791 Ma, indicating the input of mantle material into crust. Because the femic

**Table 4:** Whole-rock Sr-Nd isotopic data for the Zongnaishan granite

| Sample | $^{87}Rb/^{86}Sr$ | $^{87}Sr/^{86}Sr$ | $(^{87}Sr/^{86}Sr)_i$ | $^{147}Sm/^{144}Nd$ | $^{143}Nd/^{144}Nd$ | $\varepsilon_{Nd}(t)$ | $f_{Sm/Nd}$ | $T_{2DM}$(Ga) |
|---|---|---|---|---|---|---|---|---|
| **Zongnaishan granite** | | | | | | | | |
| 16ZN-1 | 2.35 | 0.717305 | 0.708414 | 0.1179 | 0.512209 | −0.58 | −0.40 | 1.49 |
| 16ZN-2 | 1.941 | 0.715295 | 0.707949 | 0.1120 | 0.512193 | −0.58 | −0.43 | 1.43 |
| 16ZN-3 | 2.134 | 0.715809 | 0.707734 | 0.1236 | 0.512214 | −0.58 | −0.37 | 1.58 |
| 16ZN-4 | 1.871 | 0.714963 | 0.707883 | 0.1245 | 0.512241 | −0.53 | −0.37 | 1.55 |
| 16ZN-5 | 2.109 | 0.715506 | 0.707527 | 0.1141 | 0.512207 | −0.56 | −0.42 | 1.44 |
| 16ZN-6 | 2.059 | 0.716124 | 0.708333 | 0.1166 | 0.512191 | −0.6 | −0.41 | 1.50 |

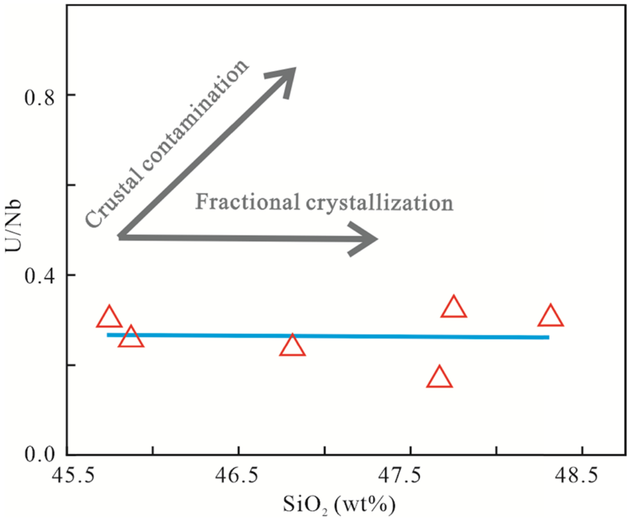

**Figure 7:** U/Nb vs $SiO_2$ diagram of the Huoersen gabbro.

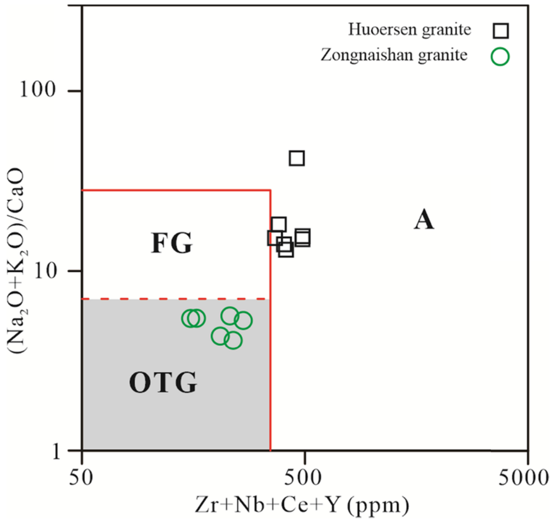

**Figure 8:** $(Na_2O + K_2O)/CaO$ vs Zr + Nb + Ce + Y diagrams of the granite [54]. FG = fractionated felsic granites; OGT = unfractionated I- and S-type granites; A = A-type granite.

constituents (MgO, $Fe_2O_3^T$) are low and because no mafic enclave was found in the sample rock, this could suggest that the mantle material was less during the magmatism process. This is obviously different from the granites of crust-mantle mixed, such as the granites of crust-mantle mixed are found in Hainan Island, China, and their most important feature was that they contain a large number of mafic enclaves [62]. The Nd/Th ratios (2.1–2.5) for Huoersen granite are close to the crustal source (3) [46], indicating that Huoersen granites are mainly the products of partial melting of the lower crust. So, the magma was derived from underplating resulting in partial melting of Neoproterozoic lower crust. The Huoersen granites have a low content of Sr and negative Eu anomalies (Figure 6e) showing the fractional crystallization of plagioclase during the process of magmatic evolution.

## 6.2 Tectonic implications

The ophiolite belts and intermediate-acidic intrusive rock in the Alxa region record a complete Paleozoic tectonic history correlated with subduction and closing of PAO. [10,19,20,22,25,27,35,37,39,63]. The ca. 300 Ma Enger Us ophiolitic mélange along the Enger Us fault belt is the oldest ophiolitic in the Alxa region and is considered the final closure site of the PAO [33,34]. The Zongnaishan-Shalazhashan tectonic zone in the south of the Enger Us fault is the product of the island arc magmatic caused by the south subduction of the PAO during the early Paleozoic, and the ca. 275 Ma Quagan Qulu ophiolitic mélange is the residual body of the back-arc basin [10,64].

In this article, the geochemical data of Huoersen gabbro (ca. 285 Ma) show enrichment of LILEs and depletion of HFSEs, indicating a tectonic setting that may directly connected with island arcs. The preceding petrogenetic analysis also supports that the gabbro originated from partial melting of lithosphere mantle that was modified by subduction metasomatic fluids. Moreover, in the Hf/3-Th-Ta and Y/15-La/10-Nb/8 diagrams (Figure 9a and b), all samples were plotted into the island arc basalt and calc-alkaline arc basalt zone. Further, the Huoersen gabbro formed in the tectonic setting of the continental marginal arc, rather than interoceanic arc. The evidences are as follows: (a) interoceanic arc is most likely to occur in the initial stage of slab subduction, and the PAO was already in the late stage of subduction during early Permian in the Alxa region [10,20,30] and (b) they display a trend of continental marginal arc in the Ce-Yb diagram (Figure 9c). The Enger Us (ca. 300 Ma) and Quagan Qulu (Ca. 275 Ma) ophiolitic mélanges sporadically outcrop along two faults in the Alxa region (Figure 1c), considered a late Paleozoic ocean-arc system [34], which only implies that the PAO did not completely disappear prior to early Permian [10,22]. Researchers have proved that ca. 281 Ma Nuergai granitoids were occurred in a subduction setting [10]. So, there was subduction of ocean in the southern Alxa region during early Permian [27]. In conclusion, the studied Huoersen gabbro was related to this subduction which was sourced from lithospheric mantle metasomatized by subduction fluids.

The Zongnaishan granite (ca. 267 Ma) belongs to I-type granite, and all samples plot in the field of volcanic arc and syn-collisional granites in the Rb-Y + Nb and Nb + Y diagram (Figure 10). Its significant depletion of Nb-Ta and

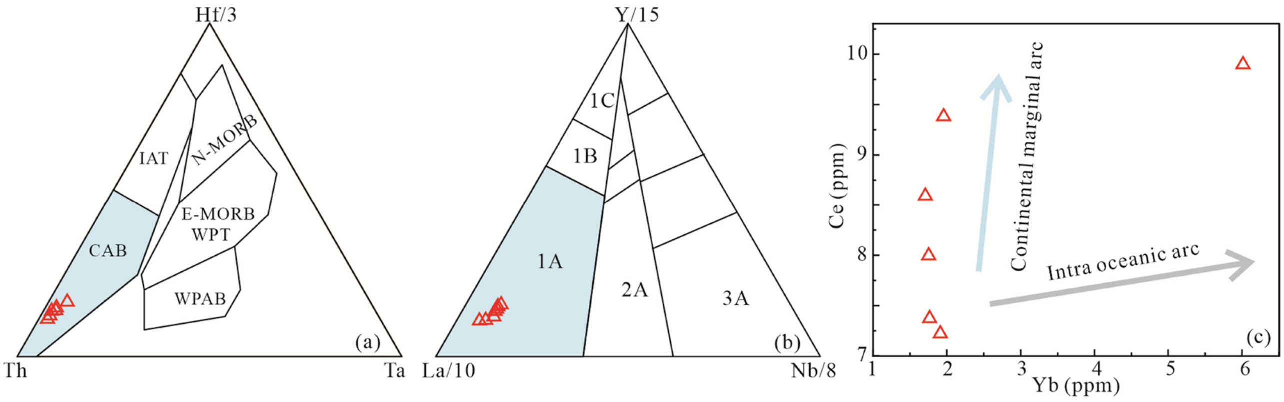

**Figure 9:** Trace element discrimination diagrams for the tectonic setting of the Huoersen gabbro. (a) Hf/3-Th-Ta diagram [76]. (b) Y/15-La/10-Nb/8 diagram [77]. (c) Ce-Yb diagram [78]. CAB – continental margin arc basalt, IAB – island arc basalt, BAB – back arc basin basalt, N-MORB – normal mid-ocean ridge basalt, E-MORB – enriched mid-ocean ridge basalt, IAT – island arc tholeiite, WPT – within-plate tholeiite, WPAB – within-plate alkali basalt, 1A – calc-alkali basalt, 1B – transition region, 1C – ocean island tholeiite, 2A – Continental basalt, 3A – alkali basalt.

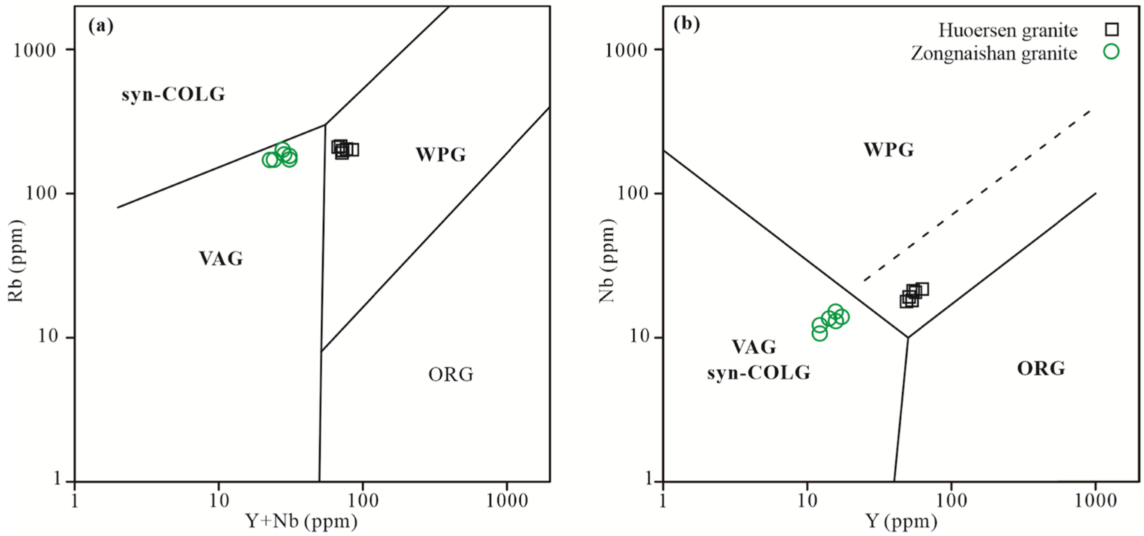

**Figure 10:** Tectonic environment discrimination diagrams of granite in the studied area. (a) Rb-Y + Nb diagram [79] and (b) Nb-Y diagram [79]. Syn-COLG – syn collisional granite, VAG – volcanic arc granite, WPG – within plate granite, POG – post-orogenic granite, ORG – oceanic ridge granite.

enrichment of LILEs (e.g., Rb, Cs, Sr, Ba) (Figure 6c) also support that they were formed in subduction environments. Geochemically, the Zongnaishan granites (A/CNK ratios of 1.01–1.13) have peraluminous characteristics of syn-collision magma and the significantly distinct low Ga/Al ratios (2.58–2.86) from the characteristic of intraplate extension setting [65] More importantly, numerous researches have suggested that the continental collision of southern Alxa region terminated at 268 Ma [10] (and references therein). Therefore, it can be concluded that Zongnaishan granites were generated in a syn-collision regime formed during the Zhusileng-Hangwula - Zongnaishan-Shalazhashan collision.

Eby [56] divided A-type granites into $A_1$ and $A_2$ subtypes. $A_1$-subtype granite source is dominated by mantle and located in intraplate or continental rift environment, while $A_2$-subtype granite source is dominated by crust, which is related to post-collision extensional environment. The Huoersen granites (ca. 259 Ma) have high Y/Nb (2.5–2.9) and Yb/Ta (4.2–4.8) ratios, indicative of $A_2$-type granites affinities [56]. Moreover, all are classified into within-plate granite in the Rb-Y + Nb and Nb-Y diagram (Figure 10). Spatially, there are lots of late Permian to early Triassic magmatic activities related to the closure of PAO and subsequently post-collision extension regime in the southern Alxa region [29,66,67]. The Huoersen granites were products of the post-collision extension setting formed after the closure of PAO.

In general, a compressional geodynamic setting shows isotopic excursion to more enriched compositions, and an extensional setting exhibits excursion to more juvenile isotopes [68–70]. In the southern Alxa region, gradually evolved isotope signatures were recorded in the magmatic rocks during the late Paleozoic (Figure 11). The late Carboniferous to early Permian magmatic rocks demonstrates decreasing $\varepsilon_{\mathrm{Nd}}(t)$ values, suggesting compression produced by the subduction of the PAO [10]. In contrast, the middle Permian to early Triassic magmatic rocks exhibit an extensional setting implied by increasing $\varepsilon_{\mathrm{Nd}}(t)$ values (Figure 11). Notably, in the transitional period of early to middle Permian (280–265 Ma), a marked shift with decentralized positive to negative $\varepsilon_{\mathrm{Nd}}(t)$ values illustrates a mixed magma source, corresponding to a tectonic switch from subduction to post-collision due to the closure of the PAO [10].

Combined with dating results of zircon U-Pb chronology and geodynamic mechanism of the studied Huoersen and Zongnaishan plutons, this paper infer that tectonic evolution of the southern Alxa region during the early Permian to late Permian involved three stages (Figure 12): a) Subduction of ocean (branch ocean of PAO) stage during ca. 285 Ma, when the Enger Us ocean southward subduction to Zongnaishan-Shalazhashan and resulted the formation of Huoersen gabbro (Figure 12a); b) Syn-collision stage during ca. 267 Ma, which means the Enger Us ocean closed during the middle Permian and formed Zongnaishan granite (Figure 12b); c) Post-collisional extensional setting during ca. 259 Ma (Figure 12c), and the asthenosphere mantle was upwelled and underplated lower crust, finally Huoersen granite were formed. The conclusion is consistent with regional magmatic events in this period.

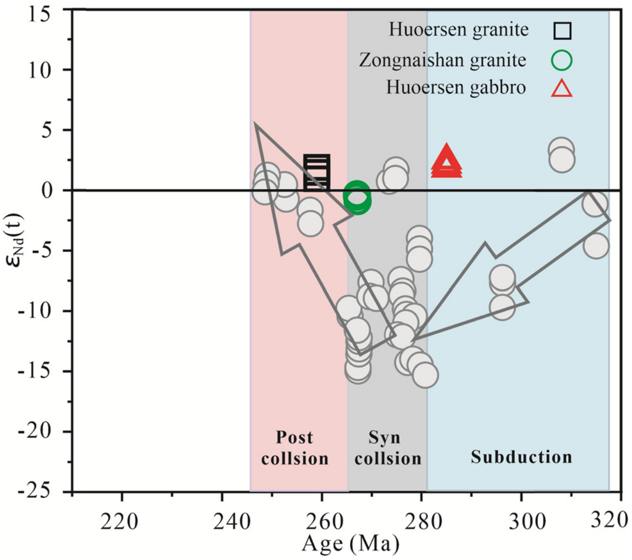

**Figure 11:** Whole-rock $\varepsilon_{\mathrm{Nd}}(t)$ values vs ages from late Carboniferous to early Triassic igneous rocks in the Alxa region. Data and arrow from [9] and the arrow indicate $\varepsilon_{\mathrm{Nd}}(t)$ values trends from Late Paleozoic igneous rocks in the Alxa region.

## 7 Conclusions

In this article, we present a petrographic, geochronological, whole-rock major and trace element, Sr-Nd-Hf isotopic data, Permian gabbro, and granite samples from the Alxa region. The major conclusions are as follows:

(1) The LA-ICP-MS zircon U-Pb age of Huoersen gabbro and granite, Zongnaishan granite, is ca. 285, 259 and 267 Ma, respectively.

(2) The calc-alkaline Huoersen gabbro is derived from the depleted mantle metasomatized by subduction fluids. The I-type Zongnaishan granite is the product of crustal remelting of Neoproterozoic. The A2-subtype Huoersen granites are the products of partial melting of the lower crust.

(3) Combined with previous studies, a model is proposed involving subduction (ca. 285 Ma), syn-collision (267 Ma), and post-collisional extension (ca. 259 Ma) for an oceanic branch of PAO in the Alxa region.

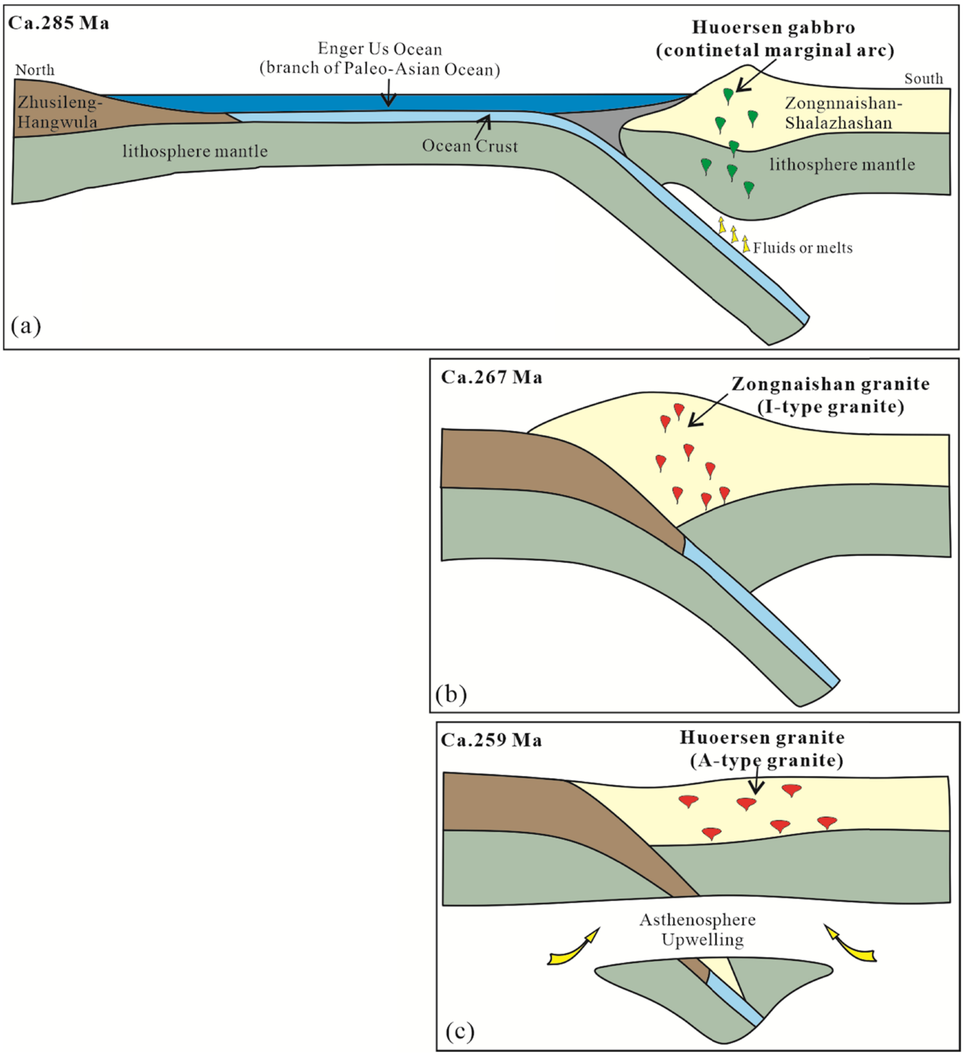

**Figure 12:** Simplified schematic model of the formation of Permian magmatic rocks in the southern Alxa region. (a) The Enger Us ocean southward subduction to Zongnaishan-Shalazhashan and resulted the formation of Huoersen gabbro. (b) Syn-collision stage, which means the Enger Us ocean closed and formed Zongnaishan granite. (c) Post-collisional extensional setting and formed Huoersen granite.

**Funding information:** This study was supported by Fundamental Research Funds for the Central Universities (lzujbky-2023-it17), the China Atomic Energy Authority (CAEA) through the Geological Disposal Program, and the National Second Tibetan Plateau Expedition Program (2019QZKK0901).

**Author contributions:** Conception, E.W., X.Z., and J.W.; methodology, E.W., X.Z., Y.H. R.S., Z.G., and C.L.; investigation, E.W., W.C., L.W., G.S., and Y.H.; data curation, E.W., W.C., L.W., G.S., and Z.G.; writing – original draft, E.W.; writing – review and editing, X.Z. and J.W.; project administration, X.Z. and J.W; and funding acquisition, E.W., X.Z., and J.W. All authors have read and agreed to the published version of the article.

**Conflict of interest:** The authors declare that there is no conflict of interest.

**Data availability statement:** Data available on request from the author.

## References

[1] Bierlein FP, Gray DR, Foster DA. Metallogenic relationships to tectonic evolution – the Lachlan Orogen, Australia. Earth Planet Sci Lett. 2002;202(1):1–13.

[2] Goldfarb RJ, Baker T, Dubé B, Groves DI, Hart CJR, Gosselin P et al. Distribution, character, and genesis of gold deposits in metamorphic terran. One Hundredth Anniversary Volume: Society of Economic Geologists; 2005. p. 105.

[3] Kröner A, Kovach V, Belousova E, Hegner E, Armstrong R, Dolgopolova A, et al. Reassessment of continental growth during the accretionary history of the Central Asian Orogenic Belt. Gondwana Res. 2014;25(1):103–25.

[4] Şengör AMC, Natal'in BA, Burtman VS. Evolution of the Altaid tectonic collage and Palaeozoic crustal growth in Eurasia. Nature. 1993;364(6435):299–307.

[5] Jahn BM, Wu F, Chen B. Granitoids of the Central Asian Orogenic Belt and continental growth in the Phanerozoic. Earth Environ Sci Trans R Soc Edinb. 2000;91(1–2):181–93.

[6] Xiao WJ, Windley BF, Huang BC, Han CM, Yuan C, Chen HL, et al. End-Permian to mid-Triassic termination of the accretionary processes of the southern Altaids: Implications for the geodynamic evolution, Phanerozoic continental growth, and metallogeny of Central Asia. Int J Earth Sci. 2009;98(6):1189–217.

[7] Windley BF, Xiao W. Ridge subduction and slab windows in the Central Asian Orogenic Belt: Tectonic implications for the evolution of an accretionary orogen. Gondwana Res. 2018;61:73–87.

[8] Dong Y, Zhang G, Neubauer F, Liu X, Hauzenberger C, Zhou D, et al. Syn- and post-collisional granitoids in the Central Tianshan orogen: Geochemistry, geochronology and implications for tectonic evolution. Gondwana Res. 2011;20(2-3):568–81.

[9] Cleven N, Lin S, Guilmette C, Xiao W, Davis B. Petrogenesis and implications for tectonic setting of Cambrian suprasubduction-zone ophiolitic rocks in the central Beishan orogenic collage, Northwest China. J Asian Earth Sci. 2015;113:369–90.

[10] Liu Q, Zhao G, Han Y, Eizenhöfer PR, Zhu Y, Hou W, et al. Geochronology and geochemistry of Permian to Early Triassic granitoids in the Alxa Terrane: Constraints on the final closure of the Paleo-Asian Ocean. Lithosphere. 2017;9(4):665–80 .

[11] Wang E, Zhai X, Chen W, Wu L, Song G, Wang Y, et al. Late devonian a-type granites from the beishan, southern central Asia Orogenic Belt: Implications for closure of the Paleo-Asia Ocean. Minerals. 2023;13(4):565.

[12] Cunningham D. Folded Basinal Compartments of the Southern Mongolian Borderland: A Structural Archive of the Final Consolidation of the Central Asian Orogenic Belt. Geosciences. 2017;7(1):2.

[13] Su B-X, Qin K-Z, Sakyi PA, Liu P-P, Tang D-M, Malaviarachchi SPK, et al. Geochemistry and geochronology of acidic rocks in the Beishan region, NW China: Petrogenesis and tectonic implications. J Asian Earth Sci. 2011;41(1):31–43.

[14] Niu Y, Liu C, Shi GR, Lu J, Xu W, Shi J. Unconformity-bounded Upper Paleozoic megasequences in the Beishan Region (NW China) and implications for the timing of the Paleo-Asian Ocean closure. J Asian Earth Sci. 2018;167:11–32.

[15] Niu Y, Shi GR, Wang J, Liu C, Zhou J, Lu J, et al. The closing of the southern branch of the Paleo-Asian Ocean: Constraints from sedimentary records in the southern Beishan Region of the Central Asian Orogenic Belt, NW China. Mar Pet Geol. 2021;124:104791.

[16] Saktura WM, Buckman S, Nutman AP, Belousova EA, Yan Z, Aitchison JC. Continental origin of the Gubaoquan eclogite and implications for evolution of the Beishan Orogen, Central Asian Orogenic Belt, NW China. Lithos. 2017;294–295:20–38.

[17] Song D, Xiao W, Windley B, Qigui M, Ao S, Wang H, et al. Closure of the Paleo-Asian Ocean in the Middle-Late Triassic (Ladinian-Carnian): Evidence from provenance analysis of retroarc sediments. Geophys Res Lett. 2021;48:e2021GL094276.

[18] Li J, Wu C, Chen X, Zuza AV, Haproff PJ, Yin A, et al. Tectonic evolution of the Beishan orogen in central Asia: Subduction, accretion, and continent-continent collision during the closure of the Paleo-Asian Ocean. GSA Bull. 2022;135(3–4):819–51.

[19] Tian R, Wang X, Ge R, Zhu W, Xie G. Early to Middle Paleozoic magmatism and metamorphism in the Alxa Block and its northern margin: Implications for the western extension of the Bainaimiao arc. Lithos. 2023;440–441:107041.

[20] Wang E-T, Zhai X-W, Chen W-F, Ma Z, Wu L, Guo Z-A, et al. Late Paleozoic tectonics of Southern Central Asian orogenic belt: Evidence from magmatic rocks in the northern Alxa, Northwest China. Front Earth Sci. 2023;10:1046122.

[21] Song D, Glorie S, Xiao W, Collins AS, Gillespie J, Jepson G, et al. Tectono-thermal evolution of the southwestern Alxa Tectonic Belt, NW China: Constrained by apatite U-Pb and fission track thermochronology. Tectonophysics. 2018;722:577–94.

[22] Liu Q, Zhao G, Sun M, Han Y, Eizenhöfer PR, Hou W, et al. Early Paleozoic subduction processes of the Paleo-Asian Ocean: Insights from geochronology and geochemistry of Paleozoic plutons in the Alxa Terrane. Lithos. 2016;262:546–60.

[23] Zhao X, Liu C, Wang J, Zhang S, Guan Y. Geochemistry, geochronology and Hf isotope of granitoids in the northern Alxa region: Implications for the Late Paleozoic tectonic evolution of the Central Asian Orogenic Belt. Geosci Front. 2020;11(5):1711–25.

[24] Xu B, Charvet J, Chen Y, Zhao P, Shi G. Middle Paleozoic convergent orogenic belts in western Inner Mongolia (China): framework, kinematics, geochronology and implications for tectonic evolution of the Central Asian Orogenic Belt. Gondwana Res. 2013;23(4):1342–64.

[25] Zhang W, Wu T, Feng J, Zheng R, He Y. Time constraints for the closing of the Paleo-Asian Ocean in the Northern Alxa Region: Evidence from Wuliji granites. Sci China Earth Sci. 2013;56(1):153–64.

[26] Chen Y, Gan L, Wu T. The Carboniferous-Permian tectonic setting for the southernmost Central Asian Orogenic Belt: Constraint from magmatic and sedimentary records in the Alxa area, NW China. Lithos. 2021;398–399:106350.

[27] Zheng R, Li J, Xiao W, Wang L. A new ophiolitic mélange containing boninitic blocks in Alxa region: Implications for Permian subduction events in southern CAOB. Geosci Front. 2018;9(5):1355–67.

[28] Shi X, Wang T, Zhang L, Castro A, Xiao X, Tong Y, et al. Timing, petrogenesis and tectonic setting of the Late Paleozoic gabbro–granodiorite–granite intrusions in the Shalazhashan of northern Alxa: Constraints on the southernmost boundary of the Central Asian Orogenic Belt. Lithos. 2014;208–209:158–77.

[29] Hui J, Zhang K-J, Zhang J, Qu J, Zhang B, Zhao H, et al. Middle–late Permian high-K adakitic granitoids in the NE Alxa block, northern China: Orogenic record following the closure of a Paleo-Asian oceanic branch? Lithos. 2021;400–401:106379.

[30] Zhang J, Zhang B, Zhao H. Timing of amalgamation of the Alxa Block and the North China Block: Constraints based on detrital zircon U–Pb ages and sedimentologic and structural evidence. Tectonophysics. 2016;668–669:65–81.

[31] Niu P, Qu J, Zhang J, Zhang B, Zhao H. Precambrian tectonic affinity of the Southern Langshan Area, Northeastern Margin of the Alxa Block: Evidence from Zircon U-Pb Dating and Lu-Hf Isotopes. Acta Geol Sin – Engl Ed. 2022;96(5):1516–33.

[32] Zhang J, Gong J, Yu S, Li H, Hou K. Neoarchean–Paleoproterozoic multiple tectonothermal events in the western Alxa block, North China Craton and their geological implication: Evidence from zircon U–Pb ages and Hf isotopic composition. Precambrian Res. 2013;235:36–57.

[33] Wang T. Great progress has been made in the study on the formation and evolution of Paleozoic lithosphere in Alashan area. J Lanzhou Univ. 1989;4:143 (in Chinese).

[34] Zheng R, Wu T, Zhang W, Xu C, Meng Q, Zhang Z. Late Paleozoic subduction system in the northern margin of the Alxa block, Altaids: Geochronological and geochemical evidences from ophiolites. Gondwana Res. 2014;25(2):842–58.

[35] Tian R, Xie G, Zhu W, Zhang J, Gao S, Zhang B, et al. Late Paleozoic Tectonic Evolution of the Paleo-Asian Ocean in the Northern Alxa Block (NW China). Tectonics. 2020;39(8):e2020TC006359.

[36] Zhang Q, Niu Y, Yao J, Zhao G, Han Y, Liu Q. Paleogeographic affinity of the Alxa Block across the Archean–Proterozoic: Insights from metamorphosed Archean basement. Precambrian Res. 2022;381:106864.

[37] Chen Y, Wu T, Gan L, Zhang Z, Fu B. Provenance of the early to mid-Paleozoic sediments in the northern Alxa area: Implications for tectonic evolution of the southwestern Central Asian Orogenic Belt. Gondwana Res. 2019;67:115–30.

[38] Deng W, Shao Z, Xu H, Chen X. Late Palaeozoic tectonic evolution of the southern Central Asian Orogenic Belt: Constraints from the Early Permian magmatism in the northern Alxa area. Geol J. 2023;58(5):1760–75.

[39] Li R-W, Zhang X, Shi Q, Chen W-F, An Y, Huang Y-S, et al. Early Permian to Late Triassic tectonics of the southern Central Asian Orogenic Belt: geochronological and geochemical constraints from gabbros and granites in the northern Alxa area, NW China. Geol Mag. 2020;157(12):2089–105.

[40] Wiedenbeck M, AllÉ P, Corfu F, Griffin WL, Meier M, Oberli F, et al. Three natural zircon Standards for U-Th-Pb, Lu-Hf, trace element and ree analyses. GeostGeoanalytical Res. 1995;19(1):1–23.

[41] Andersen T. Correction of common lead in U–Pb analyses that do not report 204Pb. Chem Geol. 2002;192(1):59–79.

[42] Luan Y, He K, Tan X. In situ U- Pb dating and trace element determination of standard zircons by LA- ICP- MS. Geol Bull China. 2019;38(07):1206–18 (in Chinese with English Abstract).

[43] Ludwig KR. ISOPLOT 3.0: A Geochronological Toolkit for Microsoft Excel. Berkeley Geochronology Center Special Publication. Vol. 39, US Geol Sur Open File Rep; 2003. p. 91–445.

[44] Tsuyoshi L, Eggins SM, McCulloch MT, Kinsley LPJ, Mortimer GE. Precise and accurate determination of 147Sm/144Nd and 143Nd/144Nd in monazite using laser ablation-MC-ICPMS. Chem Geol. 2011;282(1–2):45–57.

[45] Hoskin PWO, Schaltegger U. The composition of zircon and igneous and metamorphic petrogenesis. Rev Mineral Geochem. 2003;53:27–62.

[46] Rapp RP, Watson EB. Dehydration melting of metabasalt at 8–32 kbar: Implications for continental growth and crust-mantle recycling. J Petrol. 1995;36(4):891–931.

[47] Pearce JA, Peate DW. Tectonic implications of the composition of volcanic ARC magmas. Annu Rev Earth Planet Sci. 1995;23(1):251–85.

[48] Pearce JA. Geochemical fingerprinting of oceanic basalts with applications to ophiolite classification and the search for Archean oceanic crust. Lithos. 2008;100(1–4):14–48.

[49] Zhao J-H, Asimow P. Formation and evolution of a magmatic system in a rifting continental margin: Neoproterozoic Arc- and MORB-like dike swarms in South China. J Petrol. 2018;59(9):1811–44.

[50] Taylor SR, McLennan SM. The continental crust: Its composition and evolution. An Examination of the Geochemical Record Preserved in Sedimentary Rocks. J Geol. 1985;94(4):57–72

[51] Rudnick RL, Gao S. Composition of the continental Crust. Treatise Geochem. 2014;4:1–51.

[52] Qiu J, Wang R, Zhao J, Yu S. Petrogenesis of the early Jurassic gabbro-granite complex in the middle segment of the Gangdese belt and its implications for tectonic evolution of Neo-Tethys: A case study of the Dongga pluton in Xi'gaze. Acta Petrol Sin. 2015;31(12):3569–80 (in Chinese with English Abstract).

[53] Han B-F, He G-Q, Wang X-C, Guo Z-J. Late Carboniferous collision between the Tarim and Kazakhstan–Yili terranes in the western segment of the South Tian Shan Orogen, Central Asia, and implications for the Northern Xinjiang, western China. Earth-Sci Rev. 2011;109(3–4):74–93.

[54] Whalen JB, Currie KL, Chappell BW. A-type granites: geochemical characteristics, discrimination and petrogenesis. Contrib Mineral Petrol. 1987;95(4):407–19.

[55] Chappell BW, White AJR. I- and S-type granites in the Lachlan Fold Belt. Earth Environ Sci Trans R Soc Edinb. 1992;83(1–2): 1–26.

[56] Eby N. Chemical subdivision of the A-type granitoids:Petrogenetic and tectonic implications. Geology. 1992;20(9):641–4.

[57] King PL, Chappell BW, Allen CM, White AJR. Are A-type granites the high-temperature felsic granites? Evidence from fractionated granites of the Wangrah Suite. Australian J Earth Sci. 2001;48(4):501–14.

[58] Clemens J. S-type granitic magmas – petrogenetic issues, models and evidence. Earth Sci Rev. 2003;61(1–2):1–18.

[59] Smith DR, Noblett J, Wobus RA, Unruh D, Douglass J, Beane R, et al. Petrology and geochemistry of late-stage intrusions of the A-type, mid-Proterozoic Pikes Peak batholith (Central Colorado, USA): implications for petrogenetic models. Precambrian Res. 1999;98(3):271–305.

[60] Turner SP, Foden JD, Morrison RS. Derivation of some A-type magmas by fractionation of basaltic magma: An example from the Padthaway Ridge, South Australia. Lithos. 1992;28(2):151–79.

[61] Gao R, Xiao L, Pirajno F, Wang GC, He XX, Yang G, et al. Carboniferous–permian extensive magmatism in the West Junggar, Xinjiang, northwestern China: its geochemistry, geochronology, and petrogenesis. Lithos. 2014;204:125–43.

[62] Lv F, Xin Y, Li J, Wang J. Permian-Triassic tectonic evolution of Hainan Island: Constraintsfrom Geochronology and geochemistry of magmatic and metamorphic rocks. Acta Geol Sin. 2023;97:30–51 (in Chinese with English Abstract).

[63] Zhang Y, Zhang J, Chen X, Wang Y, Zhao H, Nie F, et al. Late Palaeozoic tectonic setting of the southern Alxa Block, NW China: constrained by age and composition of diabase. Int Geol Rev. 2017;59(8):1028–46.

[64] Wu T, He G. Ophiolitic mélange belts in the northern margin of the Alashan block. Geoscience. 1992;6(3):286–96 (in Chinese with English Abstract).

[65] Yan H, Zhu G, Chen Z, Zhang C, Hou Z, Sun Q. Geochronology and geochemistry of I-type granites in the northeastern margin of Tarim Plate. Acta Petrol Sin. 2020;36(11):3414–26 (in Chinese with English Abstract).

[66] Zhang B, Zhang J, Zhang Y, Zhao H, Wang Y, Nie F. Tectonic affinity of the Alxa Block, Northwest China: Constrained by detrital zircon U–Pb ages from the early Paleozoic strata on its southern and eastern margins. Sediment Geol. 2016;339:289–303.

[67] Xie F, Wu J, Sun Y, Wang L, Wu J, Jia W. Permian to Triassic tectonic evolution of the Alxa Tectonic Belt, NW China: Constraints from

petrogenesis and geochronology of felsic intrusions. Lithos. 2021;384–385:105980.

[68] Smits RG, Collins WJ, Hand M, Dutch R, Payne J. A Proterozoic Wilson cycle identified by Hf isotopes in central Australia: Implications for the assembly of Proterozoic Australia and Rodinia. Geology. 2014;42(3):231–4.

[69] Boekhout F, Roberts NMW, Gerdes A, Schaltegger U. A Hf-isotope perspective on continent formation in the south Peruvian Andes. Vol. 389. London: Geological Society; 2015. p. 305–21. Special Publications.

[70] Han Y, Zhao G, Cawood PA, Sun M, Eizenhöfer PR, Hou W, et al. Tarim and North China cratons linked to northern Gondwana through switching accretionary tectonics and collisional orogenesis. Geology. 2016;44(2):95–8.

[71] Zheng X, Yin H, Gao L, Wang M, Wang Y, Zhou H. Geochemical characteristics and its tectonic significance of the Early Paleozoic siliceous rocks in Hangwula area of northern Alxa. Inn Mong J Paleogeography. 2017;19(3):491–502 (in Chinese with English Abstract).

[72] Middlemost EAK. Naming materials in the magma/igneous rock system. Earth-Science Rev. 1994;37(3):215–24.

[73] Peccerillo A, Taylor SR. Geochemistry of eocene calc-alkaline volcanic rocks from the Kastamonu area, Northern Turkey. Contrib Mineral Petrol. 1976;58(1):63–81.

[74] Chappell BW, White AJR. Two contrasting granite types: 25 years later. Australian J Earth Sci. 2001;48(4):489–99.

[75] Sun SS, McDonough WF. Chemical and isotopic systematics of oceanic basalts: implications for mantle composition and processes. Geol Society, London, Spec Publ. 1989;42(1):313–45.

[76] Wood DA. The application of a Th-Hf-Ta diagram to problems of tectonomagmatic classification and to establishing the nature of crustal contamination of basaltic lavas of the British Tertiary Volcanic Province. Earth Planet Sci Lett. 1980;50:11–30.

[77] Cabanis B, Lecolle M. Le diagramme La/10-Y/15-Nb/8: un outil pour la discrimination des series volcaniques et la mise en evidence des processus de melande et/ou de contamination crustale. Space sciences. Earth sciences. 1989;309:2023–9.

[78] Hawkesworth CJ, Gallagher K, Hergt JM, McDermott F. Mantle and slab contributions in ARC Magmas. Annu Rev Earth Planet Sci. 1993;21(1):175–204.

[79] Pearce J, Harris N, Tindle A. Trace element discrimination diagrams for the tectonic interpretation of granitic rocks. J Petrol. 1984;25:956–83.